

REVEALING THE MILKY WAY'S HIDDEN CIRCUM-GALACTIC MEDIUM WITH THE COS QUASAR DATABASE FOR GALACTIC ABSORPTION LINES

Y. ZHENG¹, J. E. G. PEEK^{2,3}, M. E. PUTMAN¹, AND J. K. WERK⁴

¹ Department of Astronomy, Columbia University, New York, NY 10027, USA; yzheng@astro.columbia.edu

² Space Telescope Science Institute, 3700 San Martin Dr, Baltimore, MD 21218, USA

³ Department of Physics & Astronomy, Johns Hopkins University, 3400 N. Charles Street, Baltimore, MD 21218, USA

⁴ Department of Astronomy, University of Washington, Seattle, WA 98195-1580, USA

ABSTRACT

Every quasar spectrum contains absorption-line signatures from the interstellar medium, disk-halo interface, and circumgalactic medium (CGM) of the Milky Way (MW). We analyze *HST*/COS spectra of 132 quasars to study the significance and origin of the Si IV absorption at $|v_{\text{LSR}}| \leq 100 \text{ km s}^{-1}$. Within this velocity range, Si IV has an average column density of $\log \bar{N} = 13.50 \pm 0.17$ and its all-sky distribution does not significantly correlate with the Galactic latitude or longitude. The gas in the north predominantly infalls at $v \gtrsim -50 \text{ km s}^{-1}$ while in the south no such pattern is observed. We find that the Si IV distribution cannot be explained by the commonly adopted disk-halo model of a flat slab co-rotating with the disk. We propose a two-component model to reconstruct the distribution with a global background and a plane-parallel disk-halo component. With block bootstrapping, we find $13.41 \lesssim \log N_{\text{global}} \lesssim 13.59$ and $\log N_{\text{DH},\perp} \lesssim 12.89$ for the global and disk-halo components at 1σ , respectively. The global component is most likely to have a Galactic origin, although its exact location is uncertain. If it were associated with the MW's extended CGM, our order-of-magnitude mass estimate finds a total mass of $\sim (3.7 - 5.6) \times 10^{10} M_{\odot} (\frac{R}{160 \text{ kpc}})^2$ for gas at warm ionized phases, consistent with CGM studies of $\sim L^*$ galaxies at low redshifts. Our analyses show that there is likely to be a large amount of gas at $|v_{\text{LSR}}| \leq 100 \text{ km s}^{-1}$ hidden in the MW's CGM. Along with this work, we make our continuum-normalized spectra publicly available as the COS Quasar Database for Galactic Absorption Lines (COS-GAL).

Keywords: Galaxy: halo - Galaxy: structure - quasars: absorption lines - techniques: spectroscopic

1. INTRODUCTION

The star-forming disk of a galaxy is embedded in a massive multiphase plasma, the so called circumgalactic medium (CGM). The galaxy grows by accreting material from the CGM, while the CGM is enriched, heated, and stirred by outflows from the galaxy (Putman et al. 2012; Tumlinson et al. 2017). One of the tools proven most useful for studying the CGM of galaxies is absorption-line observations towards background quasars (QSOs), providing rest-frame observations of the multi-phase CGM with weakly (e.g., Mg II, Si II) or highly ionized metals (e.g., O VI). Significant evidence has been found for the CGM as a massive, multiphase reservoir for sub- to super- L^* galaxies at $z \lesssim 0.5$ (e.g., Chen et al. 2010; Prochaska et al. 2011; Stocke et al. 2013; Werk et al. 2014; Bordoloi et al. 2014; Liang & Chen 2014; Burchett et al. 2016; Prochaska et al. 2017; Keeney et al. 2017).

The star-forming disk and CGM are closely connected via inflows and outflows, forming an active disk-halo interface. The interface is difficult to probe due to its spa-

tial and kinematic proximity to the dense disk material and the complicated inflow and outflow interplay. For nearby extragalactic systems, the disk-halo interface can be studied in edge-on star-forming galaxies in H α or H I 21cm emission lines, often recognized as the diffuse ionized gas (DIG) or the extraplanar gas (e.g., Rand 1997, 2000; Fraternali et al. 2005; Boettcher et al. 2016). Recent galaxy surveys with integral field units (IFU), such as the SAMI Galaxy Survey (Allen et al. 2015; Ho et al. 2016) and MaNGA (Bundy et al. 2015; Bizyaev et al. 2017), also detect the disk-halo interface in H α in several dozens of edge-on nearby galaxies.

The disk-halo interface is commonly found to co-rotate with the disk. The rotation velocity of the gas at the interface gradually declines as a function of distance from a galaxy plane. This is referred to as halo lagging. Deep H I observations of edge-on galaxies in the local universe show a halo lagging of $dv_{\text{rot}}/dz \sim 15 \pm 4 \text{ km s}^{-1} \text{ kpc}^{-1}$, where z is the distance from the disk plane (Marasco & Fraternali 2011). A similar vertical falloff of $22 \pm 6 \text{ km s}^{-1} \text{ kpc}^{-1}$ is found within 100 pc of the MW's plane (Levine

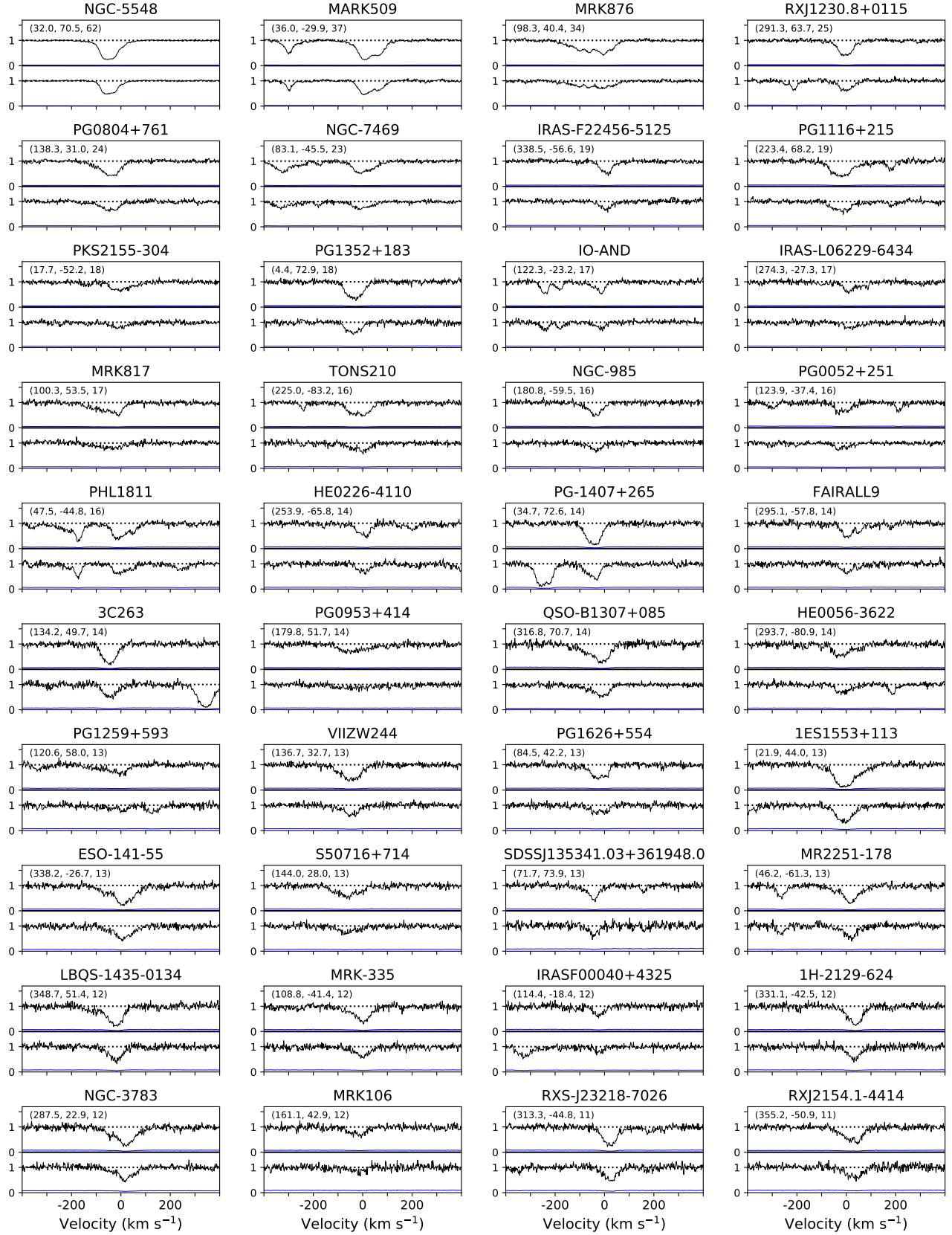


Figure 1: Continuum-normalized flux (black) and error (blue) of Si IV doublets. All the spectra are in their original spectral resolution. Each frame is noted with a QSO ID, and (Galactic longitude, Galactic latitude, SNR per pixel) in parentheses. From panel to panel, the spectra are arranged from high to low SNR per pixel. The 120 QSOs in this figure are classified as spectrally resolved with $Q = 0$, please see § 2.3 for more details.

et al. 2008). With a sample of 67 edge-on galaxies from the MaNGA survey, Bizyaev et al. (2017) found that the halo lagging scales with galaxy stellar mass: low mass galaxies ($M_* \sim 10^{9.5} M_\odot$) tend to have lower lagging with $dv_{\text{rot}}/dz \lesssim 10 \text{ km s}^{-1} \text{ kpc}^{-1}$, while massive systems ($M_* \sim 10^{10.5} M_\odot$) are more likely to have larger halo lagging with $dv_{\text{rot}}/dz \sim 40 \text{ km s}^{-1} \text{ kpc}^{-1}$.

The MW's disk-halo interface, also often referred to as the gaseous Galactic thick disk (Savage et al. 2003; Savage & Wakker 2009, hereafter SW09; Wakker et al. 2012, hereafter W12), is the only one that has been broadly observed and studied. Its multiple gas phases, temperature gradient, scale height, and kinematics are among those properties that are of great interest. The H I layer of the MW's disk has a thickness of $\leq 220 \text{ pc}$ at $R < R_\odot$ and flares dramatically beyond the solar circle (Dickey & Lockman 1990). The ionized gas with different phases occupies various vertical layers beyond the H I plane (Putman et al. 2012), usually modeled as symmetrical flat slabs with exponential density profiles (Savage et al. 1997; Savage et al. 2003; Bowen et al. 2008; SW09; W12). By investigating ionic absorption lines within $|v_{\text{LSR}}| \lesssim 100 \text{ km s}^{-1}$ seen toward MW's halo stars and background QSOs, SW09 found that the scale heights of the MW's disk-halo interface are $\sim 3 - 4 \text{ kpc}$ for Si IV, C IV, and O VI if modeled with flat slabs. We will discuss their analyses further in § 4.1. Here we note that SW09 included 15 QSOs and six stellar sightlines in the Large/Small Magellanic Clouds (LMC/SMC) to determine the flat-slab scale height, which may result in bias since it is unclear where the ionized gas lies along the line of sight toward these distant targets.

Unlike halo star spectra, every QSO spectrum contains absorption-line signatures from the MW's interstellar (ISM), disk-halo interface, and CGM. In fact, Savage et al. (2003) report that a flat slab is a poor fit to the O VI absorption-line data observed with QSO sightlines. We raise the question as to whether the QSO absorption-line measurements are suitable for MW disk-halo studies in the context of a flat slab near the Galactic disk. More specifically, we ask what the origin of the ionized gas moving at $|v_{\text{LSR}}| \lesssim 100 \text{ km s}^{-1}$ is. Although traditional studies have often associated this gas with the Galactic disk-halo, the origin remains uncertain since the distance to the gas is poorly constrained. In particular, many studies have indicated that the MW is embedded in a warm-hot medium with mass on the order of $\sim 10^{10-11} M_\odot$ out to the virial radius (e.g., Anderson & Bregman 2010; Gupta et al. 2012). Therefore, it is likely that a QSO sightline going through the MW's CGM would collect cool ion absorbers embedded in the warm-hot medium. A synthetic observation (Zheng et al. 2015) has shown that there is likely to be an equally massive amount of gas moving at low velocity as compared

to the commonly studied high-velocity gas in the MW's CGM.

Here we leverage the HST Spectroscopic Legacy Archive (HSLA; Peebles et al. 2017) to revisit the ion distribution in the Galactic disk-halo interface and halo. The HSLA dataset provides medium resolution COS spectra at G130M and/or G160M gratings. Low ions, such as C II, Si II, and Si III, are so strong that they are often fully saturated and can only be used to study the gas at $|v_{\text{LSR}}| > 100 \text{ km s}^{-1}$. For gas moving at $|v_{\text{LSR}}| \leq 100 \text{ km s}^{-1}$, usually transition lines at high-ionization stages are used, such as Al III, Si IV, C IV, and O VI (e.g., Savage et al. 2003, SW09, W12). In this work, we focus on the Si IV doublet at 1393/1402 Å to study the gas at $|v_{\text{LSR}}| \leq 100 \text{ km s}^{-1}$ over the Galactic sky. Hereafter we refer to the velocity range of $|v_{\text{LSR}}| \leq 100 \text{ km s}^{-1}$ as the *low-intermediate* velocity, and refer to the range of $|v_{\text{LSR}}| > 100 \text{ km s}^{-1}$ as the *high* velocity.

The paper is organized as follows: § 2 introduces our data reduction of the HST/COS spectra, including continuum fitting, column density and centroid velocity calculations, and evaluation of line saturation. We make our continuum-normalized spectra publicly available as described in § 2.2, and the dataset can be found here: [10.17909/T9N677]. In § 3 we study the all-sky distribution of the low-intermediate Si IV absorbers. We compare our QSO measurements with SW09's flat-slab model prediction in § 4.1, and propose a new two-component model in § 4.2. In § 5, we discuss the caveats of SW09's and our models (§ 5.1), investigate the origin of the global component (§ 5.2), and finally conduct an order-of-magnitude mass estimate for the global component in the context of the MW's CGM (§ 5.3). We conclude in § 6.

2. DATA

2.1. General Overview

We obtain our QSO spectra from HSLA (Peebles et al. 2017). The first release of HSLA (February 2017) delivers uniformly reduced and co-added HST/COS spectra with M-mode (medium-resolution/ G130M and G160M) and L-mode (low-resolution/ G140L) observations. For each target, the spectra from different programs, epochs, and gratings are co-added to improve the signal-to-noise ratio (SNR) and the wavelength coverage. HSLA arranges targets into different categories, such as *Solar System and Exoplanets*, *Stars and Galaxies and Clusters*; in this work, we make use of those spectra under the category of *QSOs, AGNs, and Seyferts*, which we will henceforth refer to as the HSLA QSO catalog.

For M-mode observations, the HSLA QSO catalog includes co-added spectra of 467 QSOs with the G130M grating and 305 QSOs with the G160M grating. In total there are 511 QSOs, among which 261 QSOs were ob-

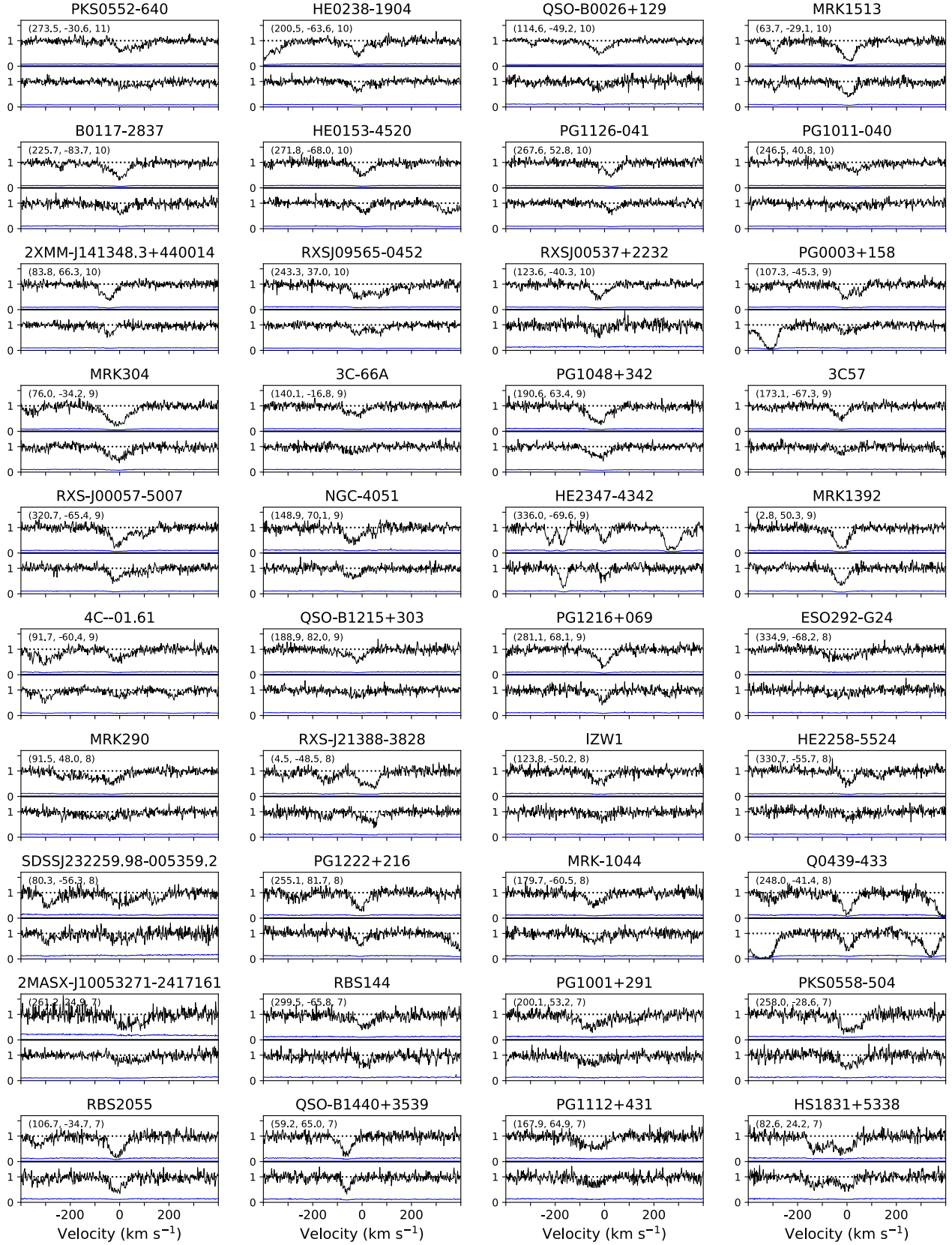


Figure 1 continued.

served with both G130M and G160M. HSLA characterizes each spectrum with an average SNR, defined as the mean of the SNR values per resolution element (taken to be six pixels) calculated over 10 \AA windows every 1000 \AA starting from 1150 \AA (Peeples et al. 2017). Our analyses focus on those QSOs with $\text{SNR} \geq 5$, which includes 385 (246) QSOs with the G130M (G160M) grating. In total there are 401 QSOs, among which 230 QSOs have both G130M and G160M observations.

For the 401 QSOs with $\text{SNR} \geq 5$, we perform continuum normalization for a series of interstellar absorption lines, including Fe II 1142/1143/1144/1608 \AA , P II 1152 \AA , S II 1250/1253/1259 \AA , Si II 1190/1193/1206/1526 \AA , Si III 1260 \AA , Si IV 1393/1402 \AA , C II 1334 \AA , and C IV 1548/1550 \AA . We focus on the spectral region within $\pm 1000 \text{ km s}^{-1}$ of the rest wavelength of each line of interest, and use Linetools¹ package (Prochaska et al. 2016) to conduct the continuum normalization. Linetools is an in-development open-source 1D spectral analysis package. Its continuum normalization function² makes use of an Akima Spline to generate the continua from absorption-free regions near the lines of interest. An interactive interface is generated for each spectrum, and we visually inspect the suggested continua and make local correction to account for higher-order continuum variation if needed. We make our dataset publicly available along with the publication of this manuscript. The details of the data release can be found in § 2.2.

2.2. Data Publication

We make our continuum-normalized COS spectra publicly available as the COS Quasar Database for Galactic Absorption Lines (COS-GAL). This database includes 401 QSOs that were observed with the G130M and/or G160M gratings. For each target, we perform continuum normalization for a number of interstellar lines, including Fe II 1142/1143/1144/1608 \AA , P II 1152 \AA , S II 1250/1253/1259 \AA , Si II 1190/1193/1206/1526 \AA , Si III 1260 \AA , Si IV 1393/1402 \AA , C II 1334 \AA , and C IV 1548/1550 \AA . We extract the spectrum within $\pm 1000 \text{ km s}^{-1}$ of the rest wavelength of each line of interest, and write the data into fits format. Each file includes the original spectral line data, the absorption-line-free continuum, the continuum-normalized flux, and the errors. Note that these continuum-normalized spectra are specifically processed to study the absorption lines associated with the ionized gas of the MW. They are not ideal for the studies of any broad features, especially those that are intrinsic to the host QSOs. Users interested in these features should examine the original spectra instead.

Along with the ion lines, we provide H I 21cm emission line spectra extracted at the position of each QSO.

We retrieve the H I 21cm lines from three H I surveys: GALFA-H I (Peek et al. 2018), HI4PI (HI4PI Collaboration et al. 2016), and LAB (Kalberla et al. 2005). GALFA-H I covers 32% of the sky with fine spatial and velocity ($4'/0.18 \text{ km s}^{-1}$) resolution, while the other two surveys are for the full Galactic sky but with lower resolution ($16.2'/1.49 \text{ km s}^{-1}$ for HI4PI and $36'/1.25 \text{ km s}^{-1}$ for LAB). We refer the reader to Table 1 in HI4PI Collaboration et al. (2016) for a comparison of the three surveys. For each QSO, we retrieve H I 21cm lines from GALFA-H I averaged over a $4'$ and a 1° beam, from HI4PI averaged over a $16.2'$ and a 1° beam, and from LAB averaged over a 1° beam.

Note that the COS spectra are observed with an aperture size of only $2.5''$, which is much smaller than the radio beam sizes of the H I surveys. Thus, we caution that the ionized gas studied by COS-GAL and the neutral gas extracted from these HI surveys may not be entirely co-spatial. We provide the HI spectra at various resolutions to partially investigate this and refer the reader to a study by Wakker et al. (2001) that examines the influence of different radio beam sizes on studies of high and low-intermediate velocity clouds.

2.3. Data Reduction Focused on The Si IV Doublet

In the following we focus on the Si IV doublet at 1393.76 \AA and 1402.77 \AA to study the warm-ionized gas associated with the MW's disk-halo and halo. These two lines are observed with the G130M gratings, therefore there are 385 QSO available in the HSLA QSO catalog. We examine the continuum-normalized Si IV doublet for each of the 385 QSOs and identify 291 QSOs with reliable absorption lines. The other 94 QSOs are mostly with unmatched absorption components, or the spectral data quality is so poor that no good judgment can be made. For the adopted 291 QSOs, we calculate the SNR per pixel for the non-absorption continuum region between 1394 \AA and 1401 \AA . We find 132 QSOs with $\text{SNR per pixel} \geq 5$, which form the core sample of our following analyses. For each spectrum, we correct the velocity to the LSR frame with

$$v_{\text{LSR}} = v_{\text{hel}} + 9\cos(l)\cos(b) + 12\sin(l)\cos(b) + 7\sin(b), \quad (1)$$

where v_{hel} is the heliocentric velocity used in the HSLA and COS spectra. In Figure 1 we show the doublet spectra of 120 QSOs that we classify as spectrally resolved with $Q = 0$, and in Figure 2 we show the spectra of nine QSOs with unresolved saturation ($Q = 1$) and three with uncertain contamination ($Q = -1$). The judgment of the line saturation and the Q value is based on the apparent column density measurements as described next.

We adopt the apparent optical depth (AOD) method (Savage & Sembach 1991, 1996) to calculate the apparent column density profiles $N_{1393}(v)$ and $N_{1402}(v)$, which is,

¹ <https://github.com/linetools/linetools>

² <http://linetools.readthedocs.io/en/latest/xspectrum1d.html>

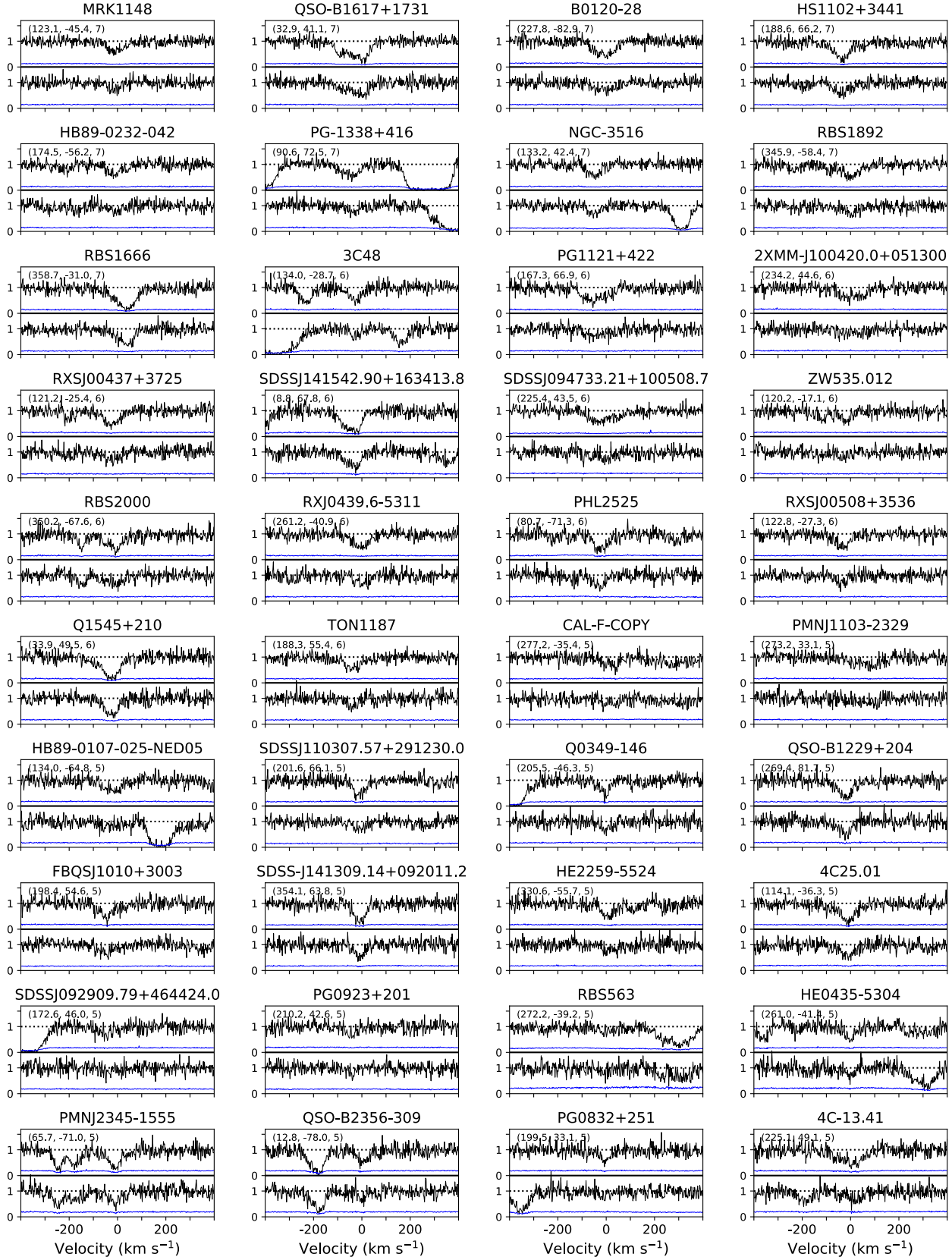


Figure 1 continued.

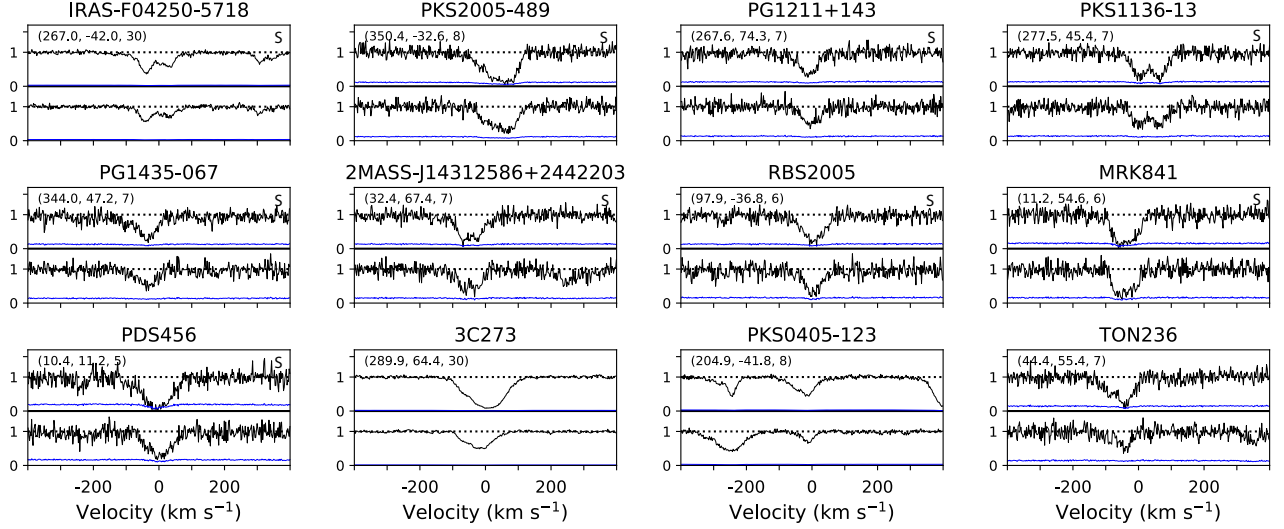


Figure 2: The first nine sightlines have unresolved saturation in the Si IV doublet, because their column density measurements do not match Eq. 4 or their normalized flux is below 0.1 (i.e., PDS456). These targets are shown in red in Fig 3 and tagged with $Q = 1$ in Table 1. The last three targets have abnormally strong Si IV 1393 Å profiles; we tag them with $Q = -1$ in the table and do not use them for future analyses. Please see § 2.3 for more details.

$$\begin{aligned}
 N_\lambda(v) &= \frac{m_e c}{\pi e^2} \frac{-\ln[F_n(v)]}{f\lambda} \\
 &= 3.768 \times 10^{14} \frac{-\ln[F_n(v)]}{f\lambda(A)} [\text{atoms cm}^{-2}(\text{km s}^{-1})^{-1}],
 \end{aligned}
 \tag{2}$$

where $F_n(v)$ is the continuum-normalized spectrum, and the wavelength $\lambda = 1393.76$ (1402.77) Å and the oscillator strength $f = 0.513$ (0.254) are adopted from Morton (2003). For both lines, we calculate the total column density and centroid velocity as,

$$\begin{aligned}
 N_\lambda &= \int_{v_-}^{v_+} N_\lambda(v) dv \\
 v_\lambda &= \int_{v_-}^{v_+} v N_\lambda(v) dv / \int_{v_-}^{v_+} N_\lambda(v) dv,
 \end{aligned}
 \tag{3}$$

where $v_- = -100$ km s⁻¹ and $v_+ = +100$ km s⁻¹, respectively. We tabulate the integrated column density and centroid velocity in Table 1.

Savage & Sembach (1991) pointed out that there might exist spectrally unresolved saturation even though the absorption line profiles appear to be shallow. This effect is most significant when the full width half maximum (FWHM) of a strong absorption line is comparable to or smaller than the FWHM of the instrument's line-spread function. The unresolved saturation can also occur if multiple absorption components with various line widths co-exist at similar velocity regions; the original absorption line profiles end up being smeared into broader but shallower profiles. Savage & Sembach (1991) suggested that for ions with more than one transition line, an efficient way to identify unresolved saturation is to compare the apparent column density profiles $N_\lambda(v)$ or the integrated apparent column density N_λ over a certain

velocity range. A well-resolved spectrum should yield consistent $N_\lambda(v)$ profiles among the multiplet absorption lines and consistent integrated N_λ values. This method has been widely used to identify smearing effect of unresolved saturation in the spectra (e.g., Howk et al. 2006; W12).

W12 identify unresolved saturation by comparing the doublet N_λ measurements for all the ions they studied, such as Si IV, N V, C IV, and O VI. They require the column density difference between the ion doublet to be within the linearly combined measurement errors. Here we adopt a similar approach, but require,

$$\begin{aligned}
 \delta \log N &\equiv |\log N_{1393} - \log N_{1402}| \leq \sigma_c, \\
 \sigma_c &\equiv (\sigma_{1393}^2 + \sigma_{1402}^2)^{\frac{1}{2}},
 \end{aligned}
 \tag{4}$$

where σ_c is the combined quadrature error of the doublet column density difference, and σ_{1393} and σ_{1402} are the measured logarithmic errors of the corresponding $\log N_{1393}$ and $\log N_{1402}$ values, respectively. Among the 132 QSOs, we identify 121 QSOs satisfying Eq. 4, suggesting that these QSOs have well resolved doublet spectra. We carefully inspect each of the spectra and find that one of the targets, PDS456, has a minimum flux of $F_n \leq 0.1$ in Si IV 1393 Å. Since COS spectra is empirically known to be saturated at this level, we classify PDS456 as spectrally saturated with $Q = 1$. Eventually we have 120 QSOs with well resolved Si IV doublet ($Q = 0$) as shown in Figure 1, and the comparison between the doublet column density measurements for $Q = 0$ targets is shown as black dots in Fig 3.

For the rest of the QSOs, we classify nine of them as

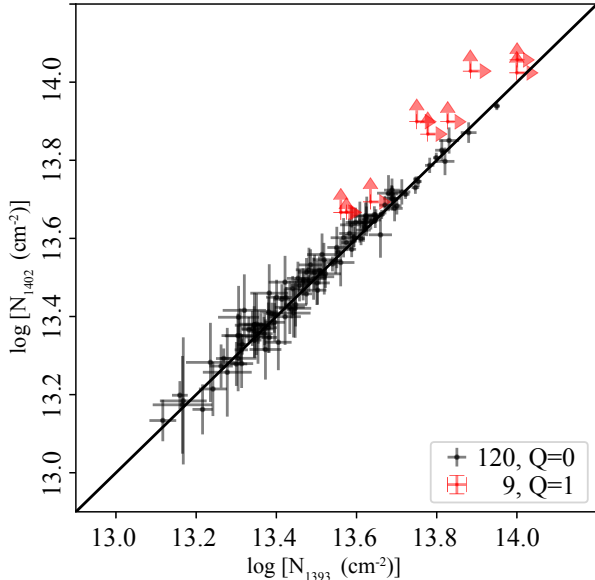


Figure 3: Comparison of Si IV doublet column density measurements. In black are the 120 QSO sightlines with spectrally resolved doublet profiles ($Q = 0$), i.e., meeting the criterion in Eq. 4. In red are the nine sightlines with unresolved saturation ($Q = 1$) in their doublet spectra (see § 2.3).

spectrally saturated with $Q = 1$ and show their doublet spectra in Fig 2. These include PDS456 which we describe above and the other eight QSOs that do not satisfy Eq. 4. The column density measurements with these QSOs are shown as red crosses in Fig 3, from which we find that saturation mostly occurs at high column densities. Savage & Sembach (1991) provide column density correction for unresolved saturation, which is based on a simulation of an isolated Gaussian component being smeared by instrument’s line-spread function with different FWHM. However, as they pointed out, the correction are most precise if the doublet’s logarithm column density difference is less than 0.05 dex; for targets with larger difference, the column density correction itself could vary up to 0.1–0.3 dex if the lines have multiple components. Given that our $\log N$ measurement errors are ~ 0.05 dex for most of the low SNR sightlines, and that the broad line profiles are probably caused by multi-components, it is unrealistic to apply SW09’s column density correction to our data. We only list the column density as lower limits for these nine QSOs in Table 1.

For the remaining three QSOs, TON236, 3C273, and PKS0405-123, we find that their Si IV 1393 Å is abnormally stronger than the 1402 Å with $\log N_{1393} > \log N_{1402} + \sigma_c$. Their spectra are shown in the last three panels in Fig 2. For 3C273, W12 suggests that the 1393 Å line may suffer from blending with Ly α . For PKS0405-

123, we measure $\log N_{1393} = 13.45 \pm 0.01$, consistent with W12’s FUSE value of $\log N_{1393} = 13.43 \pm 0.04$; note that the QSO is listed as PKS0405-12 in their work. However, for 1402 Å we find $\log N_{1402} = 13.27 \pm 0.02$ while W12 find $13.40 \pm .07$. Neither line shows signs of a peculiar profile in our COS spectra (Figure 2) despite the $\log N$ difference. As W12 did not provide the original FUSE spectra for PKS0405-123, we cannot conduct a close inspection of the line profiles to further compare results. For TON236, the 1393Å line may be contaminated by an additional line at $v_{\text{LSR}} \sim -90 \text{ km s}^{-1}$ that does not have a corresponding component at 1402 Å. For these three QSOs, we tag them as $Q = -1$, and do not use them for future analyses.

Among the 132 QSOs, we found 19 sightlines in common with the FUSE sightlines used in W12. We note these sightlines with asterisks in the first column of Table 1. Among them, 16 have spectrally resolved ($Q = 0$) doublet profiles observed with COS. For these sightlines, we calculate the integrated column density over the same velocity range as W12 adopted. We find that $\log N_{1393}$ agrees within ± 0.08 dex and $\log N_{1402}$ agrees within ± 0.09 dex, except RXJ1230.8+0115 for which our measurements show $\log N_{1393} = \log N_{1402} = 13.51 \pm 0.01$, while W12 gave $\log N_{1393} = 13.47 \pm 0.04$ and $\log N_{1402} = 13.30 \pm 0.09$. Since our doublet values are consistent and they match W12’s Si IV 1393Å value, it is likely that W12 overestimated the continuum of 1402Å for this target.

3. THE ALL-SKY DISTRIBUTION OF Si IV MOVING AT $|V_{\text{LSR}}| \leq 100 \text{ km s}^{-1}$

In this section we study the column density ($\log N$) and centroid velocity (v_c) distribution of the low-intermediate velocity Si IV over the Galactic sky, as shown in Figures 4 and 5. For each $Q = 0$ sightline, $\log N$ is the mean column densities of the doublet measurements; and for each $Q = 1$ sightline, $\log N$ is taken to be the values of $\log N_{1402}$ since Si IV 1402Å is weaker thus is less saturated. The centroid velocity v_c is the average value of the doublet measurements for each QSO regardless of the target’s Q value. Overall the north and south are roughly evenly sampled with 61 and 68 QSO sightlines, respectively. For $Q = 0$ sightlines with spectrally resolved doublet profiles, the minimum and maximum values of $\log N$ are 13.13 and 13.94, with an average of 13.50 and a standard deviation of 0.17 dex. If excluding those sightlines potentially associated with the Fermi Bubbles (see next), we find that the maximum $\log N$ is 13.78, and the rest of the sample has an average $\log N$ of 13.48 and a standard deviation of 0.15 dex. The general scatter range of Si IV is consistent with the Si IV measurements by W12 using FUSE spectra (see their Figure 7).

We find a $\log N$ enhancement towards the Galactic center near $|l| \lesssim 30^\circ$ and $-40^\circ \lesssim b \lesssim 80^\circ$, which roughly

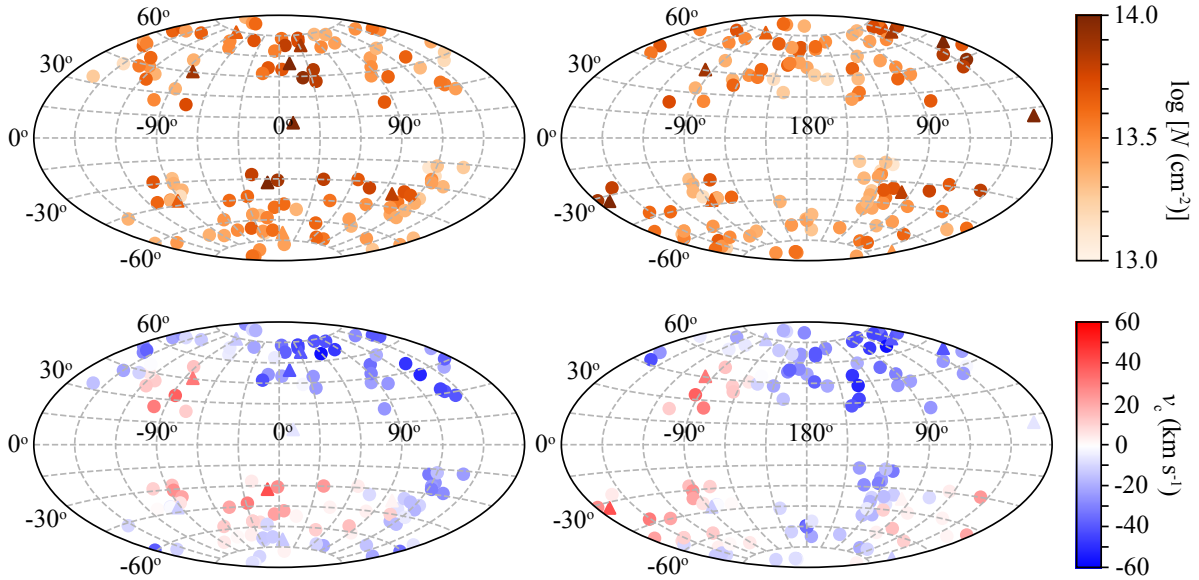


Figure 4: The top two panels show the all-sky distribution of the Si IV column density integrated from -100 to $+100$ km s^{-1} , with the left panel centered at the Galactic center and the right panel at anti-Galactic center. For each spectrally resolved sightline ($Q = 0$, dots), we show the mean column density of the doublet; and for each saturated sightline ($Q = 1$, upward triangles), we show the column density of $\log N_{1402}$ as the lower limit, given that Si IV 1402\AA is weaker thus is less saturated than 1393\AA . The bottom two panels show the distribution of the centroid velocity v_c over the sky, which is the mean centroid velocity of the doublet regardless of a target’s Q value (see § 3).

coincides with the Fermi Bubbles (Ackermann et al. 2014; Fox et al. 2015; Bordoloi et al. 2017). Sightlines within this region have $\log N$ generally ~ 0.2 dex higher than others as is better shown in panel (1a) in Figure 5, although the centroid velocities are not significantly different. There are 14 sightlines that are likely to be associated with the Fermi Bubbles, which are indicated with † in Table 1. Ten of these sightlines are in common with the sightlines used for the study of the north Fermi Bubble by Bordoloi et al. (2017). One of them, PDS456, lies inside the Fermi Bubble at $l = 10.4^\circ$ and $b = 11.2^\circ$. Our AOD analyses show that the Si IV doublet of this sightline are saturated (see § 2.3) with $\log N \geq 14.02$, while Bordoloi et al. (2017) gave a consistent estimate of $\log N > 14.05$ based on Voigt profile fitting (see also Fox et al. 2015 for a detailed study of PDS456 through the Galactic center). The other nine sightlines all lie outside of the north Fermi Bubble but generally within $10^\circ - 20^\circ$ of the bubble boundaries.

Except for these 14 sightlines, we find that the $\log N$ distribution in the north and south are similar as shown in Figures 4 and 5. This is different from the observations of the low-intermediate velocity O VI in the Galactic halo as studied by Savage et al. (2003). There they found that the O VI column density at $b > 45^\circ$ is ~ 0.25 dex higher than other regions of the Galactic sky.

Kinematically, we find that in the north a significant

fraction of the Si IV-bearing gas is moving towards us at $v_c \gtrsim -50$ km s^{-1} , as seen from the centroid velocity distribution in Figures 4 and 5. The blue-shifted pattern near $l \sim 180^\circ$ cannot be simply explained by co-rotation or halo lagging of ionized gas at the MW’s disk-halo interface, which would otherwise show a clear segregation pattern of blue- and red-shifted velocity at $l = 180^\circ$ (Wakker 2004). As most sightlines are at high Galactic latitudes, their centroid velocities suffer only modest projection effects. The blue-shifted gas in the north implies an excess of inflowing gas toward the disk. In the south, no obvious trend of gas inflows is found.

We detect Si IV absorption along every COS sightline studied in this work, indicating the low-intermediate velocity Si IV has a covering fraction (i.e., detection rate) of $C_f = 100\%$ over the Galactic sky at $|b| \gtrsim 30^\circ$. This is very different from the results of the ionized high-velocity gas (Fox et al. 2006; Shull et al. 2009; Collins et al. 2009; Lehner et al. 2012; Richter et al. 2017). For example, Shull et al. (2009) show that the HVC sky coverage is $81\% \pm 5\%$ based on a search of Si III absorbers in *HST*/COS and *FUSE* spectra of 37 AGNs, while Richter et al. (2017) found a covering fraction of 74% for high-velocity Si III using COS observations. Collins et al. (2009) nevertheless found a very high detection rate of $91\% \pm 4\%$ for Si III using *HST*/STIS archival data. With a different set of ions (e.g., C II, C IV, Si III, Si IV),

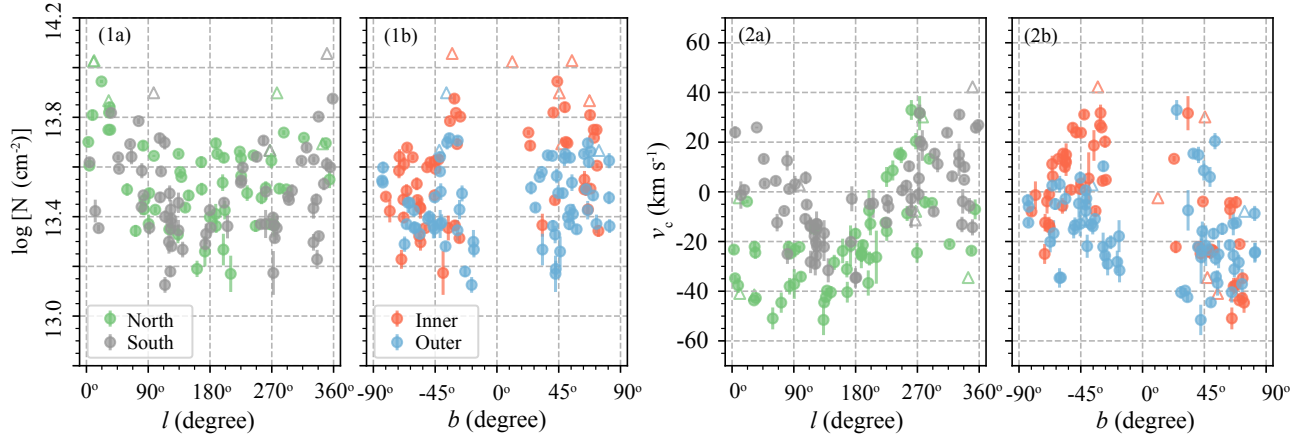


Figure 5: Panels (1a) and (1b) show the $\log N$ distribution as functions of Galactic longitude (l) and latitude (b), respectively. For $Q = 0$ sightlines, we calculate the mean value of the doublet column density (dots); for $Q = 1$ sightlines, we show the $\log N_{1402}$ value as the lower limits (upward triangles). In panel (1a), we color-code the data into North ($b > 0^\circ$, green) and South ($b \leq 0^\circ$, grey); in panel (1b), we split the data into Inner ($0^\circ < l < 90^\circ$ or $270^\circ < l < 360^\circ$, red) and Outer ($90^\circ < l < 270^\circ$, blue). Panels (2a) and (2b) show the v_c distribution as functions of l and b ; the symbols are color-coded the same way as those in panel (1a) and (1b), respectively. The centroid velocity is the mean of the doublet measurements for both the spectrally resolved and saturated sightlines.

Lehner et al. (2012) found a covering fraction of 68% for gas moving at $|v| > 90 \text{ km s}^{-1}$ at $|b| > 20^\circ$. The non-unity covering fraction of the ionized high-velocity gas can also be inferred from our doublet spectra (Figures 1 and 2), where not every sightline has absorption features at $|v| > 100 \text{ km s}^{-1}$.

4. MODELS FOR THE ALL-SKY DISTRIBUTION OF Si IV

Without distance constraints, it is difficult to trace the origins of the Si IV-bearing gas. The spectrum of a QSO sightline going through the Galactic halo is likely to contain absorption line information from the ISM, disk-halo interface, and the MW’s CGM in a large volume simultaneously. A number of authors attribute the QSO-probed Galactic Si IV to the MW’s disk-halo interface with a plane-parallel flat slab geometry (e.g., Savage et al. 1990; SW09; W12), assuming that there is very small amount of low-intermediate velocity Si IV existing in the MW’s CGM. In § 4.1, we briefly review SW09’s flat-slab model for the Galactic Si IV moving at low-intermediate velocities. Then in § 4.2, we propose a better-fit model to the data with a global component that is likely to resemble the contribution of the MW’s CGM.

4.1. A Commonly Adopted Flat Slab Model

SW09’s flat-slab model assumes a simple physical scenario that most of the Galactic Si IV at $|v| \lesssim 100 \text{ km s}^{-1}$ concentrated on the MW’s disk-halo interface. The flat slab has an exponential density profile, $n(z) = n_0 e^{-|z|/z_h}$, extending above and below the Galactic disk. In this

equation, z is the vertical distance from the Galactic plane, z_h is the scale height of the gas, and n_0 is the mid-plane number density. z_h and n_0 can be constrained in the following way: for a star at height z_s from the Galactic plane, the modeled column density seen towards the star projected along the vertical direction is $N_{\text{mod},\perp} = \int_0^{z_s} n(z, X) dz$. $N_{\text{mod},\perp}$ can then be related to the observed column density towards the star as $N_{\text{mod},\perp} = N_{\text{obs}} \sin|b|$, where b is the star’s Galactic latitude. Since the number density of the flat slab drops dramatically above z_h , the value of $N_{\text{mod},\perp}$ flattens as we probe background stars at vertical distances much larger than z_h . For extragalactic targets, such as QSO sightlines and stars in LMC/SMC, the flat-slab model expects that the Si IV column densities measured along these sightlines should be consistent with those of halo stars at distances much higher than z_h .

SW09 conducted a thorough study of the flat-slab model for the warm-hot ionized gas moving at low-intermediate velocities. They searched the literature and collected the column densities of a number of ions (e.g., H I, Al III, Si IV, C IV, O VI) for 109 halo star sightlines and 30 QSO sightlines from a number of authors (e.g., Jenkins 1978; Lehner & Howk 2007; Bowen et al. 2008; W12; see table 2 of SW09 for a complete list of references). Different authors have varied choices of velocity ranges over which the ion column densities were integrated, but the adopted ranges are all near $[-100, 100] \text{ km s}^{-1}$. For example, Bowen et al. (2008) calculated the O VI AOD column densities within $\pm 120 \text{ km s}^{-1}$ for all their stellar sightlines while W12 deliberately determined

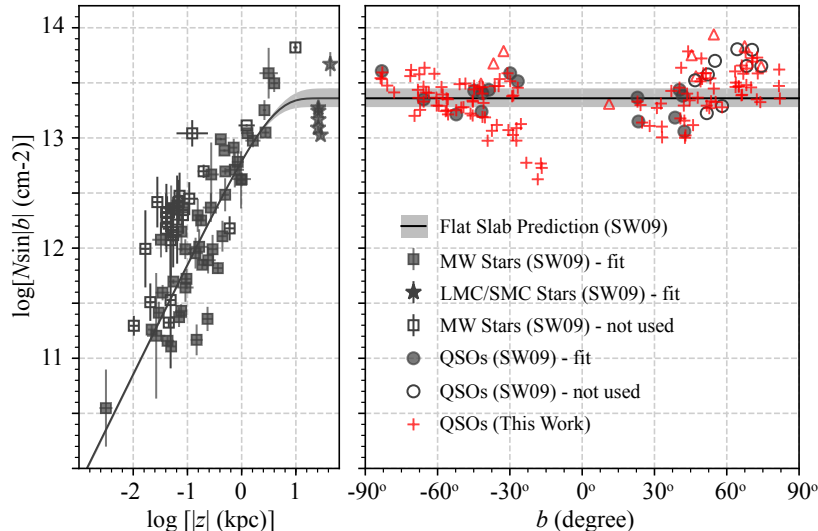


Figure 6: The $\log(N\sin|b|)$ - $\log|z|$ relation on the left panel for stellar sightlines, and $\log(N\sin|b|)$ - b on the right for QSO sightlines, respectively. The black symbols are those used by [SW09](#): filled symbols were used in their flat-slab model fitting, while open symbols were excluded due to sightlines intercepting specific ISM/halo structures. See § 4.1 for more details. This plot is adopted from their Si IV panel of Figure 2 in [SW09](#), although we do not include their upper/lower limit data. The black curve and gray shaded regions show the predicted $\log N_{\text{mod},\perp}$ and 1σ from [SW09](#)'s flat-slab model. The red crosses/upward triangles are our Si IV measurements of resolved ($Q = 0$)/saturated ($Q = 1$) sightlines, respectively; error bars are approximately equal to the size of the symbol. Our QSO data show that $\log(N\sin|b|)$ increases as $|b|$ increases, which cannot be explained by the flat slab geometry.

the velocity range of each absorption line for every QSO they used.

[SW09](#) examined the $\log(N_{\text{obs}}\sin|b|)$ - $\log|z|$ relation, and found that $\log(N_{\text{obs}}\sin|b|)$ increases with $\log|z|$ for most of their halo star sightlines but the relation reaches a plateau for stars beyond certain heights. We reproduce [SW09](#)'s flat-slab experiment using their published stellar/QSO Si IV data, which are shown as black symbols in Figure 6. In the left panel, the filled black symbols show the stellar sightlines used in their flat slab parameter fitting, including 44 MW halo stars (shown in filled squares) broadly distributed from $\log|z| \sim -2.5$ to ~ 0.5 and six LMC/SMC stellar sightlines (shown in filled stars) at $\log|z| \sim 1.7$. Sightlines noted as open symbols were not considered in their fitting due to either prominent H II regions, X-ray sources, or supernova remnants along the lines of sight. They also excluded a halo star vZ 1182 at $\log|z| \sim 1.0$ and $b \sim 79^\circ$ because of the concern of contamination from the potential excess region near the north Galactic pole, as revealed by the O VI all-sky distribution ([Savage et al. 2003](#)). The right panel shows the QSO measurements as a function of Galactic latitude b . The 15 QSOs shown in filled black circles were used by [SW09](#) for the flat slab modeling, and there are ten QSO sightlines at $b > 45^\circ$ (open circles) that were discarded to avoid the O VI-enhanced region near the north Galactic pole ([Savage et al. 2003](#)). [SW09](#)'s data show that

the value of $\log(N_{\text{obs}}\sin|b|)$ peak at ~ 13.3 for stars at $z \sim 5 - 10$ kpc (i.e., $\log|z| \gtrsim 0.5$), and the QSO measurements scatter around this value. The straight line and shaded area spanning from the left to right panels in Figure 6 show the model prediction of the $\log N_{\text{mod},\perp}$ - $\log|z|$ relation from [SW09](#)'s flat slab model. They found a best-fit scale height of $z_h = 3.2_{-0.6}^{+1.0}$ kpc and mid-plane density of $n_0 = 2.3 \times 10^{-9} \text{ cm}^{-3}$ for the Si IV flat slab.

[SW09](#)'s flat-slab model reproduces the general trend of the projected Si IV column densities seen towards halo stars and a number of QSO sightlines at $b < 45^\circ$. However, as we populate the Galactic sky with more QSO measurements shown in red crosses (resolved, $Q = 0$) and upward triangles (saturated, $Q = 1$) in the right panel of Figure 6, we find that the flat slab cannot describe the $\log(N_{\text{obs}}\sin|b|)$ - b trend as revealed by our large QSO sample. A Spearman test between $\log(N_{\text{obs}}\sin|b|)$ and $|b|$ find a correlation coefficient of $r_s = 0.53$, implying $\log(N_{\text{obs}}\sin|b|)$ is likely to increase monotonically with $|b|$. A separate test for north- and south-only sightlines finds $r_{s,n} = 0.54$ and $r_{s,s} = 0.50$. Since the flat-slab model regards QSO sightlines as those with path lengths of infinity, the $\log(N_{\text{obs}}\sin|b|)$ values from QSOs should always be $\log(N_{\text{obs}}\sin|b|) = \log(n_0 z_h) = 13.36$ ([SW09](#)). The monotonic $\log N_{\text{obs}}\sin|b|$ - $|b|$ trend indicates that a flat-slab geometry with an exponential density distribution is not adequate to explain the Si IV content along

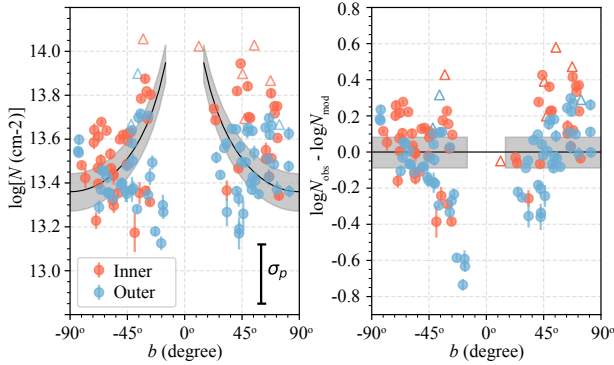


Figure 7: Left: $\log N$ - b relation for the low-intermediate Si IV from our QSO data. The data points are the same as those in panel (1b) of Figure 5. Black curves show SW09’s flat-slab model prediction, and the gray shades are the 1σ ranges. The $\sigma_p=0.27$ dex in the bottom right is the patchiness parameter that SW09 adopted, which we discuss in § 4.2. Right: Residuals of the observed and model-predicted Si IV column densities, $\delta\log N = \log N_{\text{obs}} - \log N_{\text{mod}}$. A good model fit should yield a random distribution of $\delta\log N$ around 0.0 dex, however, the actual residuals show that the flat-slab model overpredicts the $\log N$ value at low b and underpredicts those at high b .

the QSO sightlines, which we discuss in more detail next.

The mismatch between our QSO measurements and SW09’s flat-slab model prediction is further illustrated in Figure 7, where we directly compare the column density values without the $\sin|b|$ projection. The data points in the left panel are the same as those in panel (1b) of Figure 5. The black curves and gray shades show the $\log N$ prediction from SW09’s best-fit flat slab model: a QSO sightline at $b = 30^\circ$ would have twice as much column density as a QSO at $b = 90^\circ$. However, our measurements of $\log N$ show no such strong dependence on b . We find that $\log N$ generally fluctuates between 13.1 to 14.0 dex regardless of their b value. The right panel shows the column density residuals $\delta\log N$ between our measurements and SW09’s flat-slab model prediction. A good model fit should yield residuals that randomly scatter around 0.0 dex, which is not the case here. The flat slab model over-predicts $\log N$ at low b and under-predicts those sightlines at high b , resulting in an increasing $\delta\log N$ at higher b .

We note that this mis-match between the measured $\log N$ and flat-slab prediction has also been found in studies of Galactic O VI (Figure 12 of Savage et al. 2003) and C IV (Figure 8 of W12) moving at low-intermediate velocities. In their work, Savage et al. (2003) analyzed *FUSE* spectra of 100 extragalactic targets and pointed out that a symmetrical flat slab with an exponential density profile cannot accurately depict the overall distribution of O

VI moving at $|v| \lesssim 100 \text{ km s}^{-1}$. They also found that the O VI centroid velocities do not fit into the scenario of a flat slab co-rotating with the Galactic disk. C IV is likely to be a better proxy than O VI for Si IV given their comparable ionization potentials (33eV for Si IV and 48eV for C IV). In the flat-slab model, SW09 found a scale height of $z_h = 3.6$ kpc for C IV, which is similar to Si IV’s scale height of 3.2 kpc. W12 show their $\log N$ measurements of C IV at low-intermediate velocity in their Figure 8, overplotted with SW09’s flat-slab predictions. Their northern sightlines show a similar data-model mismatch to what we show in Figure 7. Their southern sightlines follow the general trend of the flat slab; however, since they only have 13 sightlines in the south, it is hard to clearly declare a $1/\sin|b|$ effect.

To briefly summarize, we find a flat-slab geometry cannot accurately describe the overall distribution of the Si IV moving at low-intermediate velocities as seen from QSO sightlines. In the following section, we proceed with a new model for the Si IV distribution by adding in a global component to the flat slab model. Then we further discuss the caveats of SW09’s flat-slab model and our model in § 5.1.

4.2. A New Two-Component Model

The flat-slab model predicts a strong dependence of $\log N$ on b , i.e., QSO sightlines near the pole regions have the shortest path lengths through the flat slab and thus should have the least Si IV, while those near the Galactic plane would have the longest paths and thus the most Si IV (see left panel of Figure 7). However, the observed $\log N$ does not follow this predicted trend closely – $\log N$ seems to have a flat, but scattered distribution from low to high b . Inspired by this b -independent distribution, here we propose a new model which includes two column density components along each QSO sightline: a disk-halo component resembling SW09’s flat slab, and a global component indicating a constant column density background. We refer to this model as the *two-component* model in the following text. The model expects the total column density for a given line of sight to be:

$$N_{\text{tot}} = N_{\text{DH},\perp}/\sin|b| + N_{\text{global}}, \quad (5)$$

where b is the Galactic latitude, $N_{\text{DH},\perp}$ represents the projected Si IV column density as predicted by a flat slab, and N_{global} is contributed by a global background. At low latitudes, the material at the disk-halo interface dominates the column densities owing to a substantially increased path length through it (a factor of 2 for gas at $b = 30^\circ$ compared to $b = 90^\circ$). Thus, the $N_{\text{DH},\perp}$ term provides an excellent description of the bulk of the material at low Galactic latitudes. At higher Galactic latitudes, the uniformly distributed global component N_{global} provides a relatively larger contribution to the

observed total column density owing to the shorter path length through the disk-halo flat slab.

Solving Eq. 5 is a straight line fit to the data in the linear $N-1/\sin|b|$ space, where $(N_{\text{DH},\perp}, N_{\text{global}})$ are the coefficients we are solving for. We use the 120 QSOs sightlines that have spectrally resolved Si IV doublets ($Q = 0$). Excluding the nine sightlines with saturated profiles ($Q = 1$) will not change our results significantly given that the quantity is small and that they are mostly at $|b| > 30^\circ$. We discuss further in § 5.1 how low- b data may affect our fitting. We conduct a linear chi-square fit to the data by minimizing $\chi^2 = \sum_{i=1}^{120} \left(\frac{N_i - N_{\text{fit}}}{\sigma_m}\right)^2$, where N_i is the measured total column density for each sightline and N_{fit} is the corresponding fit. $\sigma_m \equiv (\sigma_i^2 + \sigma_p^2)^{1/2}$ is the combined quadrature error of the measured column density error σ_i and an artificially introduced term σ_p . Since σ_i is much smaller ($\sim 10^{11-12} \text{ cm}^{-2}$; $\lesssim 0.05$ dex) than the scatter of column density (see Fig 5) which has a standard deviation order of magnitude higher ($3.15 \times 10^{13} \text{ cm}^{-2}$; 0.17 dex), we include the σ_p to regulate the χ^2 minimization so that the fitting will not be driven by those high-quality data points with the smallest σ_i .

The introduction of σ_p is inspired by the fitting method adopted by SW09. In their work, a similar σ_p was incorporated into the measurement errors so that the reduced χ^2 could be forced to 1.0 at their best fits. Their derived σ_p has a value of 0.27 dex as shown in Figure 7. Without σ_p , the reduced χ^2 would be $\gg 1.0$ and the best-fit parameters would be determined by those measurements with the smallest errors. As they emphasized, σ_p measures the degree of patchiness in the data, which is a remedy for the over-simplified model setup that has a smooth density distribution. Our two-component model suffers the same problem that it is inadequate to describe the patchiness/clumpiness of the intervening ionized gas. Physically we expect σ_p to reflect the column density variation from sightline to sightline, thus it is given the value of the standard deviation of our column density measurements at $\sigma_p = 3.15 \times 10^{13} \text{ cm}^{-2}$, or 0.17 dex for logarithmic column densities. This is consistent with SW09's choice of σ_p .

We conduct bootstrapping on the data to estimate the confidence level of the $(N_{\text{DH},\perp}, N_{\text{global}})$ solution. This is done by randomly sampling the data sightlines with replacements, and running the linear chi-square fit on every experiment so that a distribution of $N_{\text{DH},\perp}$ and N_{global} can be obtained. Although our data have sampled the north (61 QSOs) and south (68 QSOs) sky quite evenly (§ 3), it is possible that some sightlines are correlated at certain spatial scales given the large neutral/ionized HVC structures seen in the Galactic halo (van Woerden et al. 2004; Putman et al. 2012). For example, as we show in § 3, there are 14 sightlines toward the Galactic center with enhanced column densities that are likely to

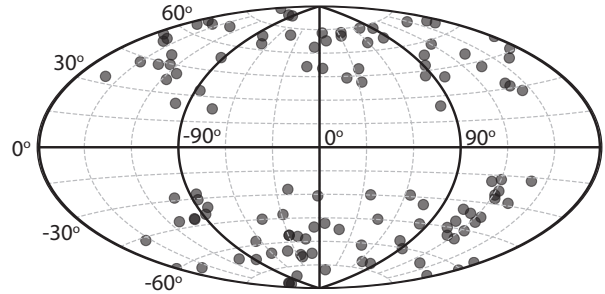


Figure 8: The distribution of the 120 QSOs with spectrally resolved Si IV profiles ($Q = 0$). Black lines divide the sky into the eight segments, which we use in block bootstrapping in § 4.2. From top left to bottom right in clockwise order, the number of sightlines in each segment is 19, 7, 13, 16, 11, 21, 12, 21, respectively.

be associated with the Fermi Bubbles. Bootstrapping on the original sample may not be able to break the degeneracy introduced by these structures. Therefore we perform block bootstrapping by dividing the Galactic sky into octants as shown in Figure 8. The selection of $90^\circ \times 90^\circ$ segments is for two reasons. First, the spatial extensions of the prominent H I HVCs and IVCs are at similar scales (van Woerden et al. 2004; Putman et al. 2012). Second, by bootstrapping these eight segments, we efficiently test how the $N_{\text{DH},\perp}$ and N_{global} values are influenced by those sightlines with the lowest or highest column densities in certain regions. We also run block bootstrapping by dividing the data sample into smaller segments (e.g., $30^\circ \times 30^\circ$, $45^\circ \times 45^\circ$, or $60^\circ \times 60^\circ$), and find smaller uncertainties of the fitting parameters as we show in Figure 9. Therefore, the octant block bootstrapping serves as the most conservative estimates on how underlying structures could affect our estimates.

Figure 9 shows our result of block bootstrapping on octants. In panel (1a/1b/3c), we show the 1D and 2D histograms of $(N_{\text{DH},\perp}, N_{\text{global}})$ solutions obtained from 10^5 block bootstrapping experiments. The data are binned in step of 10^{12} cm^{-2} for both $N_{\text{DH},\perp}$ and N_{global} . f_{2d} is defined as the fraction of experiments within each bin, which can also be interpreted as the probability that a certain $(N_{\text{DH},\perp}, N_{\text{global}})$ value is taken. Panel (1b) and (1c) show the marginal probability distribution for $N_{\text{DH},\perp}$ and N_{global} , respectively. The disk-halo component $N_{\text{DH},\perp}$ shows a double-peak distribution while the global component N_{global} has a broad base with a peak at $\sim 3.6 \times 10^{13} \text{ cm}^{-2}$. As we explain in Eq. 5, the $N_{\text{DH},\perp}$ becomes prominent at low b where $1/\sin|b|$ becomes larger, while at high b the N_{global} dominates the total column density. Therefore, the peaks at $N_{\text{DH},\perp} \sim 0$ and $N_{\text{global}} \sim 3.6 \times 10^{13} \text{ cm}^{-2}$ are likely to be caused by sampling on blocks that contain sightlines at low b with

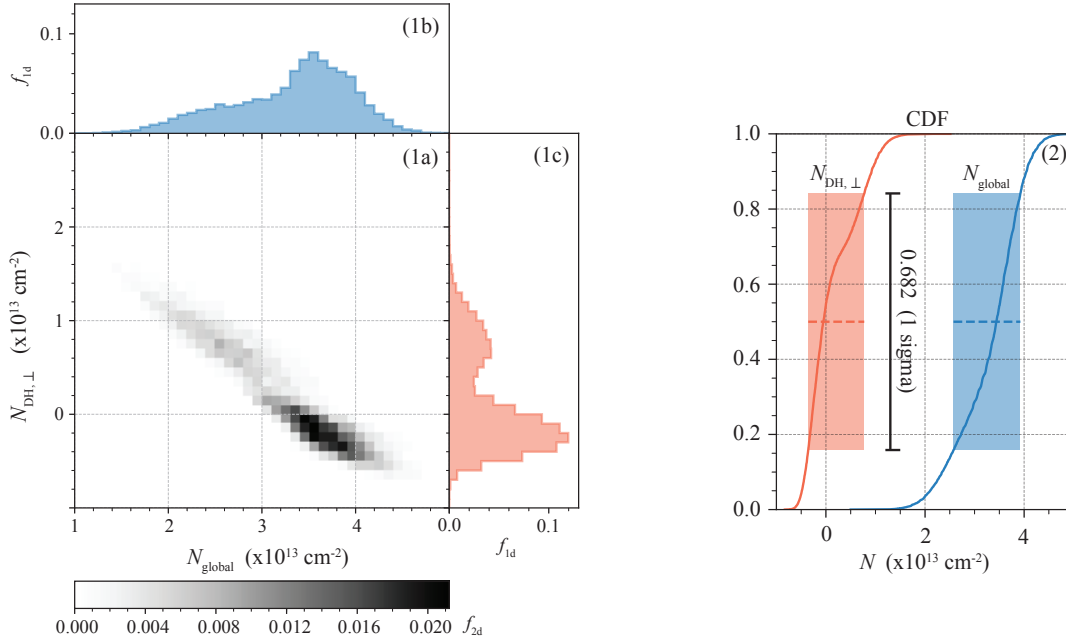


Figure 9: (1): 1D and 2D histograms of the $(N_{\text{DH},\perp}, N_{\text{global}})$ solutions drawn from 10^5 block bootstrapping experiments. Panel (1a) shows the fraction of experiments within each bin in step size of 10^{12} cm^{-2} . Panel (1b) shows the marginal probability distribution for the global component and (1c) for the disk-halo component. (2): the cumulative distribution function for the global component (blue, right) and for the disk-halo component (red, left). The square patches shows the 1σ (68.2% confidence) range of the N_{global} and $N_{\text{DH},\perp}$ values.

low column density measurements, where the model fitting strongly disfavors the disk-halo contribution. On the other hand, the second peak at $N_{\text{DH},\perp} \sim 0.7 \times 10^{13} \text{ cm}^{-2}$ and the corresponding low-value N_{global} bump result from sampling on blocks with sufficient low- b sightlines with high column density measurements, thus the fitting favors more disk-halo contribution.

We show the cumulative distribution functions (CDF) of $N_{\text{DH},\perp}$ and N_{global} in the right panel of Figure 9. At CDF = 0.5, we find a median value of $N_{\text{DH},\perp} = -5.2 \times 10^{11} \text{ cm}^{-2}$ and $N_{\text{global}} = 3.4 \times 10^{13} \text{ cm}^{-2}$. At the 68.2% confidence level we find $N_{\text{DH},\perp} \lesssim 7.7 \times 10^{12} \text{ cm}^{-2}$ and $2.6 \times 10^{13} \lesssim N_{\text{global}} \lesssim 3.9 \times 10^{13} \text{ cm}^{-2}$. These equal to $\log N_{\text{DH},\perp} \lesssim 12.89$ and $13.41 \lesssim \log N_{\text{global}} \lesssim 13.59$. The negative values of $N_{\text{DH},\perp}$ do not have physical implications on the properties of the Galactic halo medium. However, they suggest that our QSO sample might not have enough sightlines at low Galactic latitudes (e.g., $|b| < 30^\circ$) to effectively study the disk-halo component $N_{\text{DH},\perp}$, which is a caveat we will discuss in § 5.1.

In Figure 10, we compare the column density prediction of the two-component model with the QSO measurements. The data symbols are the same as those in Figure 7. The black line shows the predicted total column density from the median value drawn from the 10^5 bootstraps at each b , while the gray shades show the corresponding 68.2% confidence range. Although $N_{\text{DH},\perp}$ and

N_{CGM} show broad distribution (see Figure 9), they together produce tight N_{tot} value regulated by the straight line fit in Eq. 5. In general our two-component model can recover the Si IV column density distribution over the Galactic sky, despite the large scatter of the column densities. As we describe previously, the large scatter is most likely due to the patchy nature of the halo medium, which is accounted for by the patchiness parameter σ_p in our model. Notably, the prominent b -dependent column density residuals found in SW09’s flat-slab model (Figure 7) now mostly disappears.

Since our two-component model does not have distance information, the exact locations of the disk-halo and global components are ambiguous. In § 5.2, we discuss the potential origin(s) of the global component. For the disk-halo component, it is by design to represent the flat-slab geometry as adopted in SW09 as well as to reflect the observational evidence of the flat disk-halo interface seen in nearby edge-on galaxies (e.g., Rand 1997, 2000; Fraternali et al. 2005; Boettcher et al. 2016). For this component, we compare the model-predicted $\log N_{\text{DH},\perp}$ value with SW09’s stellar data in Figure 11. From the block bootstrapping we find that at 1σ the disk-halo component has $N_{\text{DH},\perp} < 7.7 \times 10^{12} \text{ cm}^{-2}$ or $\log N_{\text{DH},\perp} \lesssim 12.89$; this is shown as the dark-blue patch in Figure 11. For stellar sightlines within this range, we find that the maximum height is $\log|z| \sim 0$ or $|z| \sim 1 \text{ kpc}$. The light-

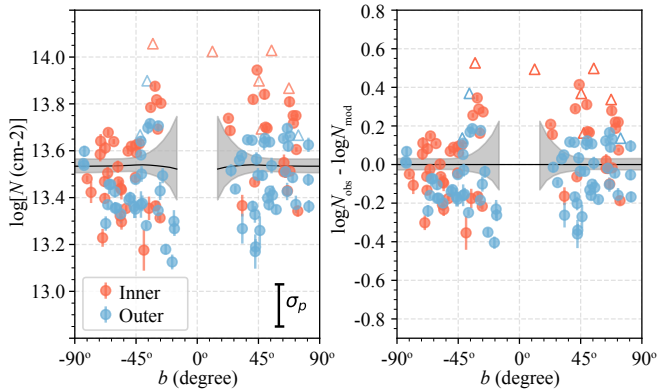


Figure 10: Left: $\log N$ - b distribution. The data points are the same as those in Figures 5 and 7. The black line shows the median values of $\log N_{\text{tot}}$ as predicted by the two-component model based on block bootstrapping. The gray shades indicate the 68.2% (1σ) confidence range as inferred from the CDF (Figure 9). The $\sigma_p = 0.17$ dex in the bottom right is the patchiness parameter used in the two-component model fitting to account for the scatter of $\log N$ (see § 4.2). Right: column density residuals of the observed and model-predicted Si IV column densities, $\delta \log N = \log N_{\text{obs}} - \log N_{\text{mod}}$. Note that the abnormal trend of $\delta \log N$ increasing with larger b as shown in Figure 7 has now disappeared, implying that our two-component model is likely a better representation of the Si IV seen towards QSOs than the commonly adopted flat-slab model.

blue patch shows the 3σ value of $\log N_{\text{DH},\perp} \lesssim 13.20$ dex, within which the highest star is at $\log |z| \sim 0.5$ or $|z| \sim 3$ kpc. This implies that our two-component model is able to reproduce the column densities towards stars within 3 kpc. Stellar sightlines beyond this height and those in the LMC/SMC start to collect more Si IV associated with the global component along the sightline path.

5. DISCUSSION

In the previous section, we briefly reviewed SW09’s flat-slab model and proposed a two-component model to better describe the all-sky distribution of Si IV absorption at low-intermediate velocity. Here, we first discuss the caveats of both models (§ 5.1). We proceed by discussing the potential origin(s) of the Si IV global component, which dominates over the disk-halo component in column density (§ 5.2). Finally, we conduct order-of-magnitude mass calculations for the global component in the context of the MW’s CGM (§ 5.3).

5.1. Caveats of the Models

A considerable degree of column density scatter can be seen in both SW09’s star/QSO sample and our QSO sample, indicating that the Si IV-bearing gas is patchy. There

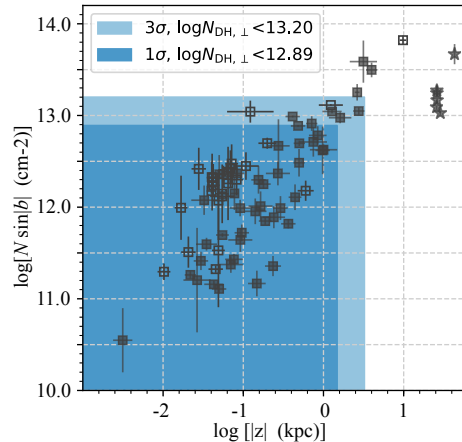


Figure 11: Comparisons between the predicted disk-halo component $\log N_{\text{DH},\perp}$ and the observed values $\log(N_{\text{obs}} \sin|b|)$ towards SW09’s stellar sightlines. The data symbols are the same as those in the left panel of Figure 6. The dark-blue patch shows the 1σ range of $\log N_{\text{DH},\perp}$ as we derive from the CDF in Figure 9, and the light-blue patch shows the 3σ range. The boundaries of the patches on the x axis are determined by the stars with the higher $\log |z|$ within each patch.

are several reasons why a disk-halo and halo medium would be patchy. For example, the Galactic fountain (Shapiro & Field 1976) that circulates material between the disk and halo may be responsible for some of the scatter. Along the trajectory of a fountain gas parcel, the gas may experience several phase changes due to different cooling rates at different locations (Marasco et al. 2012), resulting in a clumpy and inhomogeneous medium.

The patchiness parameter σ_p adopted by both SW09’s and our models is designed to account for the column density scatter. The inclusion of σ_p is to ensure that the χ^2 minimization algorithm would not be driven by those few data points with the most accurate measurements. However, the value of σ_p itself does not convey any deep physical meaning. Ideally, a comprehensive model would include a physically-motivated parameter that independently describes the clumpiness or volume filling factor. Unfortunately, our current dataset offers no insight as to what such a parameter’s true value may be and determining its value is beyond the scope of this work.

The second caveat pertaining to both SW09’s and our model is rooted in the sample selection. The halo stars in SW09 lie mostly at $|b| < 15^\circ$ and towards the inner Galaxy direction. Their sightlines at higher Galactic latitudes consist of 15 QSOs at $b < 45^\circ$ and six stars in the LMC/SMC. Along the QSO and LMC/SMC stellar sightlines, the sources of and distances to the foreground low-intermediate velocity absorbers are not well-constrained. This inhomogeneous sample selection and

the inclusion of distant sightlines likely overestimate the flat-slab scale height. In contrast, our sample is dominated by QSOs at $|b| \gtrsim 30^\circ$ and our two-component model does not have distance information on the gas as limited by the QSO data sample. Although our disk-halo component can predict most of column densities measured toward SW09’s halo stars within 3 kpc (Figure 11), ideally one should combine the QSOs and halo stars together to provide better constraints on the locations of the disk-halo and global components.

5.2. Origin(s) of the Si IV Global Component

Here we discuss the origin(s) of the global component revealed in § 4.2. We attempt to consider all of the possible ionized structures that the QSO paths may intercept.

First, we consider a Galactic ISM origin. It is unlikely that our QSO sightlines would suffer strong contamination from dense spiral-arm regions or warps at the outskirts of the MW’s disk since the QSOs are mostly at $|b| \gtrsim 30^\circ$. However, all sightlines must leave the disk through the Local Bubble, a cavity in the ISM at the location of the Sun with a radius of ~ 100 pc. SW09’s halo star sample contains three objects within 1 kpc of the Sun (HD_38666, HD_52463, HD_116658). The mean Si IV column density measured along these sightlines is $\log N \sim 12.5$ dex, which accounts for only $\sim 10\%$ of the Si IV toward distant QSOs. Furthermore, Savage & Lehner (2006) found that the local bubble contributes only $\sim 9\%$ of column density to the total O VI content in the MW halo by comparing UV spectra of nearby white dwarfs at a mean distance of ~ 109 pc with those of MW halo stars. Based on this result, SW09 suggest that Si IV from the local bubble would not have a significant effect, despite the potential phase difference between the O VI- and Si IV-traced material.

Second, superbubbles breaking out of the ISM near the solar neighborhood are unlikely to be the source. This is primarily because the upstreaming material should be found with mostly positive radial velocities, in stark contrast with our velocity centroid measurements (Figure 4) that predominantly trace negative radial velocities. However, it is possible that we are seeing the remnants of a past superbubble break-out, where the bulk of the previously-ejected material is now falling back down. In this scenario, the fall-back gas is not distinguishable from the observed ionized IVCs and HVCs, which we will discuss shortly.

Third, as our sightlines cover most of the Galactic sky at $|b| \gtrsim 30^\circ$, any particular substructures covering small areas of the sky cannot be the dominant sources, but are likely to contribute to the column density scatter. The potential structures include: (1) the Fermi Bubbles (e.g., Fox et al. 2015; Bordoloi et al. 2017) which we have discussed in § 3, (2) the CGM of M31 in the southern

sky (Lehner et al. 2015), and (3) cool filamentary structures embedded in the $10^5 - 10^7$ K warm-hot intergalactic medium in the Local Group (e.g., Nicastro et al. 2003; Richter et al. 2017). As we divide the sky into octants for block bootstrapping, the influence of sightlines potentially associated with small-area structures have been reflected in the distribution of the $(N_{\text{DH},\perp}, N_{\text{global}})$ solutions (Figure 9).

Fourth, we consider that the global component may be associated with the widespread HI structures observed in the inner Galactic halo. IVCs are defined as discrete H I clouds moving at $|v| < 100$ km s $^{-1}$ (van Woerden et al. 2004; Albert & Danly 2004; Wakker 2004) at distances of $\sim 1 - 5$ kpc above the Galactic plane (see Table 2 in Albert & Danly 2004), and HVCs are those moving at $|v| > 100$ km s $^{-1}$ at further distances around ~ 10 kpc (van Woerden et al. 2004; Putman et al. 2012; Lehner et al. 2012; Richter et al. 2017). Since we only consider the origin of the Si IV global component at low-intermediate velocities, ionized HVCs themselves are not the possible culprits; however, clouds have been found with similar properties to HVCs moving at lower velocities (Peek et al. 2009; Saul et al. 2014) as expected from models (Wakker 1991). If the global component represents the ionized counterparts of the IVCs or HVCs, one would expect the Si IV-bearing clouds to be distributed in a spherical configuration so that the column densities have minimal dependence on $|b|$.

Ultimately, we consider that the global component may represent a contribution from material occupying the MW’s CGM, extending to $\sim 0.5 R_{\text{vir}}$. All QSO sightlines would intercept the extended CGM material of the MW. The MW’s CGM is typically studied at high velocities ($|v| > 100$ km s $^{-1}$) to avoid contamination from more nearby low-intermediate velocity gas (e.g., Fox et al. 2006; Shull et al. 2009; Collins et al. 2009; Lehner et al. 2012; Richter et al. 2017). However, Zheng et al. (2015) found that $\sim 65\%$ of the MW’s CGM mass above $|b| \geq 20^\circ$ is likely to be hidden at $|v| \leq 100$ km s $^{-1}$ regardless of the gas phase, based on a synthetic observation of a simulated MW-mass galaxy from a cosmological simulation (Joung et al. 2012). Empirically, as found in extragalactic CGM studies, highly ionized, metal-enriched gas can extend to nearly half the virial radii of the host galaxies with centroid velocity largely within $|v| \lesssim 150$ km s $^{-1}$ of the systemic velocities of host galaxies (e.g., Werk et al. 2014; Liang & Chen 2014; Burchett et al. 2016). Therefore, it is likely that the Si IV in the MW’s CGM extends beyond the inner Galactic halo and casts absorption features at low-intermediate velocity ranges.

To summarize, we find that the global component is unlikely to be dominated by the Local Bubble, superbubble breakouts, Fermi Bubble, M31’s CGM, or the

Local Group medium. The global component is most likely to represent the ionized counterparts to nearby IVCs/HVCs, and/or the MW's extended, ionized CGM that occupies a much larger volume, although its exact location is unknown. In each of these potential scenarios, spherical-like geometry better describes the data than the flat-slab cylindrical geometry since there is not an observed dependence on $|b|$ for the Si IV column densities (Figures 5, 7, and 10). The dominant global component over the disk-halo component shows that there is likely to be a large amount of ionized gas moving at low-intermediate velocities hidden in the MW's CGM.

5.3. Order-of-Magnitude Calculation of the MW's CGM Mass

In this section, we conduct an order-of-magnitude calculation for the mass of the low-intermediate velocity Si IV-bearing gas in the context of the MW's CGM. We provide two mass estimates: one adopts a radius of 160 kpc (i.e., $\sim 0.5 R_{\text{vir}}$) under the assumption that the MW's CGM is similar to that of $\sim L^*$ galaxies studied at lower redshifts (e.g., Werk et al. 2014; Liang & Chen 2014; Keeney et al. 2017; Prochaska et al. 2017); the other limits the radius to 30 kpc under the assumption that the global component traces the ionized IVC/HVC counterparts in the inner Galactic halo.

5.3.1. MW's extended CGM within $R = 160$ Kpc

We first consider the case that the global component is associated with MW's extended CGM in a spherical volume with $R = 160$ kpc, a value based on the impact parameters probed by the COS-Halos survey (Tumlinson et al. 2011; Werk et al. 2014; Prochaska et al. 2017). We consider a uniform distribution of the global component with a covering fraction of $C_f = 1$, given that the detection rate of Si IV is 100% in our observations (§ 3). Note that this assumption is unlikely to be realistic since the Galactic halo is often found to be clumpy with large column density scatter (see § 3 and § 4). The Si IV mass at low-intermediate velocities is,

$$\begin{aligned} M_{\text{SiIV,low}} &= 4\pi R^2 C_f m_{\text{Si}} N_{\text{global}} \\ &= (1.9 - 2.8) \times 10^6 M_{\odot} \left(\frac{C_f}{1}\right) \left(\frac{R}{160 \text{ kpc}}\right)^2, \end{aligned} \quad (6)$$

where m_{Si} is the mass of a silicon atom, $4\pi R^2$ is the area of the spherical surface, and N_{global} is the surface density which is taken to be the column density of the global component. The range in the parentheses is based on the 1σ lower and upper values of N_{global} as derived in § 4.2.

We can further convert the Si IV mass into a hydrogen mass by assuming that the Si IV-bearing gas represents

the bulk property of the MW's CGM at cool phases:

$$\begin{aligned} M_{\text{H,low}} &= \left(\frac{M_{\text{SiIV,low}}}{m_{\text{Si}}}\right) 1.4 m_{\text{H}} f_{\text{SiIV}}^{-1} (\text{Si}/\text{H})_{\odot}^{-1} Z^{-1} \\ &= (2.4 - 3.6) \times 10^{10} M_{\odot} \\ &\quad \left(\frac{C_f}{1}\right) \left(\frac{R}{160 \text{ kpc}}\right)^2 \left(\frac{f_{\text{SiIV}}}{0.4}\right)^{-1} \left(\frac{Z}{0.3 Z_{\odot}}\right)^{-1}, \end{aligned} \quad (7)$$

where 1.4 is to account for the presence of helium and m_{H} is the mass of a hydrogen atom. We adopt $(\text{Si}/\text{H})_{\odot} = 10^{-4.49}$ from Asplund et al. (2009), which is the silicon abundance in the present-day solar photosphere relative to hydrogen. We assume the metallicity as $Z = 0.3 Z_{\odot}$, based on the COS-Halos mean CGM metallicity estimate (Prochaska et al. 2017). The most uncertain term is the ionization fraction f_{SiIV} , defined as the ratio of the Si IV to all the silicon in various neutral and ionized states. Photoionization, collisional ionization, and other non-equilibrium processes such as shock ionization, conductive interfaces, and turbulence mixing may contribute to producing Si IV (e.g., Fox et al. 2005; W12). As we only aim for an order-of-magnitude mass calculation, we do not conduct sophisticated ionization modelings to determine f_{SiIV} . Based on a collisional ionization model of Gnat & Sternberg (2007), we adopt $f_{\text{SiIV}} = 0.4$ which is the maximum ionization fraction of Si IV at $Z = 0.1 Z_{\odot}$. This is the closest ionization data to our adopted $Z = 0.3 Z_{\odot}$ value from Gnat & Sternberg (2007)'s ionization models. We also examine the ionization fraction produced by CLOUDY (v13.03; Ferland et al. 1998, 2013) in an extragalactic UV background (Haardt & Madau 2001) at H I column density of 10^{20} cm^{-2} . We find f_{SiIV} peaks at ~ 0.3 for $Z = 0.1 - 0.3 Z_{\odot}$, similar to the collisional ionization prediction by Gnat & Sternberg (2007).

Based on the synthetic observation of a simulated MW-mass galaxy, Zheng et al. (2015) found that the mass ratio of the high to low-intermediate velocity gas in the MW halo at $|b| \geq 20^{\circ}$ is 0.35:0.65 and this mass ratio does not vary significantly from 10 kpc to 250 kpc. If we apply this ratio to the calculated mass in Eq. 6 and 7, we find that the total Si IV and hydrogen mass in the MW's CGM is,

$$\begin{aligned} M_{\text{SiIV,all}} &= M_{\text{SiIV,low}}/0.65 = (2.9 - 4.3) \times 10^6 M_{\odot} \\ M_{\text{H,all}} &= M_{\text{H,low}}/0.65 = (3.7 - 5.6) \times 10^{10} M_{\odot}, \end{aligned} \quad (8)$$

Our mass calculation for the MW's extended CGM is accurate only as an order-of-magnitude estimate. We caution the Si IV ionization fraction is highly uncertain without fully understanding its ionization mechanism (e.g. W12; Werk et al. 2016). Furthermore, metallicity measurements for the ionized gas are notoriously difficult to obtain. Large systematic uncertainties in gas ionization state, metallicity and medium clumpiness plague all mass estimates based upon ionized gas absorption lines. When compared to the literature, we find that our de-

rived mass of the MW’s extended CGM is comparable to the most recent CGM mass estimates from the COS-Halos team (Prochaska et al. 2017), who found that the total mass of the cool, photoionized CGM of $L \sim L^*$ galaxies at redshift ~ 0.2 is $9.2 \pm 4.3 \times 10^{10} M_{\odot} (\frac{R}{160 \text{ kpc}})^2$. On the other hand, our estimated CGM value is higher than the mass of M31’s CGM as recently placed by Lehner et al. (2015). They derived a total Si mass of $M_{\text{Si}} = 2.1 \times 10^6 M_{\odot} (\frac{R}{50 \text{ kpc}})^2$ by considering Si II, Si III, and Si IV simultaneously. This corresponds to a total hydrogen mass of $\sim 4 \times 10^9 (\frac{R}{160})^2 (\frac{Z}{0.3 Z_{\odot}})^{-1}$ adopting our assumption of the metallicity. Note that they assumed solar metallicity for the CGM of M31.

Our mass calculation is different from the one used by Stocke et al. (2013) who estimated the CGM mass of late-type galaxies with a volume filling factor of 3%–5%. Briefly, they determined the volume filling factor of warm CGM clouds by taking into account the cover fraction, the average number of ion absorption components along the sightlines, and the physical cloud sizes as inferred from photoionization modelings (see their Eq. 5). The total CGM mass was derived by summing up the mass of all available clouds with the assumption that the warm clouds represent the whole CGM cloud population. Werk et al. (2014) calculated the CGM mass for the COS-Halos sample with both the surface density method (as we adopt here) and the volume-filling method. With a volume filling factor of 11%, they found consistent CGM mass results between the two methods. The volume-filling method has two requirements: (1) an estimate of cloud sizes based on CLOUDY modeling, and (2) an estimate of the average number of ion absorption components along the sightlines based on Voigt-profile fitting. Since neither of these is used in this work, we are unable to conduct mass estimate with the volume-filling method.

5.3.2. MW’s inner CGM within $R=30$ Kpc

Here we consider the scenario that the global component is associated with the gas in the inner Galactic halo, potentially related to the ionized counterpart of H I IVCs/HVCs. Since the Galactic disk extends out to ~ 25 kpc as observed in H I (Levine et al. 2006), here we adopt a spherical volume with $R = 30$ kpc to ensure the inclusion of the entire disk. Adopting Eq. 6 but with a smaller radius, we find $M_{\text{SiIV,low}} = (6.6 - 9.9) \times 10^4 M_{\odot} (\frac{R}{30 \text{ kpc}})^2$ at 1σ . To convert it to the hydrogen mass, we again assume $Z = 0.3 Z_{\odot}$ and $f_{\text{SiIV}} = 0.4$, and find $M_{\text{H,low}} \sim (0.9 - 1.3) \times 10^9 M_{\odot} (\frac{R}{30 \text{ kpc}})^2 (\frac{f_{\text{SiIV}}}{0.4})^{-1} (\frac{Z}{0.3 Z_{\odot}})^{-1}$. If we apply the same mass ratio of high to intermediate-velocity gas of 0.35:0.65 (Zheng et al. 2015), the hydrogen mass of the high-velocity gas in the inner Galactic halo is $M_{\text{H,high}} \sim (4.6 - 6.9) \times 10^8 M_{\odot} (\frac{R}{30 \text{ kpc}})^2$ and the total mass of the gas at all velocities is $M_{\text{H,all}} \sim (1.3 - 2.0) \times 10^9 M_{\odot} (\frac{R}{30 \text{ kpc}})^2$.

This mass calculation has the caveat that we assume a spherical volume centers at the Sun instead of the Galactic center. This caveat is negligible for the calculation in § 5.3.1 since a much larger volume is assumed, but becomes nontrivial here for a spherical volume with $R = 30$ kpc. We adopt this 30 kpc value to ensure that most of the ionized gas near the Galactic disk is taken into account; however, the mass could be overestimated by including too much volume beyond the disk. The same caveat exists in Lehner et al. (2012)’s method of estimating the total mass of ionized HVCs in the Galactic halo. They adopted a spherical volume of 12 kpc, and found $M_{\text{iHVCs}} = 1.1 \times 10^8 M_{\odot} (\frac{d}{12 \text{ kpc}})^2 (\frac{C_t}{0.5}) (\frac{Z}{0.2 Z_{\odot}})^{-1}$. A radius of 12 kpc from the Sun would result in a spherical volume directly cutting through the Galactic disk, which may not represent the real distribution of gas clouds in the inner Galactic halo.

6. CONCLUSION

For MW absorption-line studies that rely on background QSOs, the lines of sight unavoidably intercept the ISM, the disk-halo interface, and the CGM of the Galaxy. Therefore every QSO spectrum contains mixed absorption-line features from these sources. High velocity gas ($|v| > 100 \text{ km s}^{-1}$) is traditionally assumed to relate to the CGM, while low-intermediate velocity gas ($|v| \leq 100 \text{ km s}^{-1}$) is considered to be more nearby. In this work, we study the all-sky distribution and origins of the Si IV-bearing gas at low-intermediate velocity with co-added G130M COS spectra of 132 QSOs obtained from HSLA (Peeples et al. 2017). Our results are summarized as follows.

First, we find that the Si IV column density $\log N$ does not significantly correlate with the Galactic latitude or longitude, except sightlines near the Fermi Bubbles (see § 3). For other directions, we find similar $\log N$ distributions in the north and south. As for the centroid velocity v_c , we find most sightlines in the north show gas moving at negative velocities toward the LSR at $v_c \gtrsim -50 \text{ km s}^{-1}$, which implies potential inflow. Sightlines in the south do not show such velocity preference.

Second, we compare our Si IV column density measurements with the predicted values from SW09’s flat-slab model (§ 4.1). The flat slab has an exponential density profile along the direction perpendicular to the Galactic plane. We find that the column density residuals between the QSO data and the model prediction show strong dependence on the Galactic latitude, which cannot be explained by the assumed plane-parallel geometry. The flat-slab model overestimates the column densities of sightlines at low Galactic latitudes and underestimates those at high Galactic latitudes.

We propose a two-component model which consists of a disk-halo and a global component in § 4.2. The

disk-halo component $N_{\text{DH},\perp}$ is assumed to follow the flat-slab geometry, thus the line of sight column density scales with $1/|\sin|b|$. The global component N_{global} represents a general background that contributes identically from sightline to sightline in the homogeneous case. We conduct block bootstrapping to solve for the values of the disk-halo and global components, and find $\log N_{\text{DH},\perp} \lesssim 12.89$ and $13.41 \lesssim \log N_{\text{global}} \lesssim 13.59$ at 1σ . Our two-component model is able to reproduce the column density distribution seen towards distant QSOs and those stellar sightlines within 3 kpc of the Galactic plane.

We examine the potential origin(s) of the global component in § 5.2, and find that it is most likely to be associated with the MW's CGM, although its exact location is difficult to constrain without distance measurements. We conduct order-of-magnitude mass estimates for the global component with two different volume assumptions. If the global component exists in a large volume with $R = 160$ kpc, we find that the MW's extended CGM has a total hydrogen mass of $(3.7 - 5.6) \times 10^{10} M_{\odot}$ (§ 5.3.1); this mass estimate is roughly consistent with the CGM mass of $L \sim L^*$ galaxies at low redshifts. If the global component were related to the inner Galactic halo within 30 kpc, we find a total mass of $(1.3 - 2.0) \times 10^9 M_{\odot}$; note that this value might be overestimated since we assume a spherical volume from the Sun (see § 5.3.2). Our analyses of the low-intermediate velocity Si IV absorbers and the two-component model show that there is likely to be a large amount of ionized gas moving at low-intermediate velocity hidden in the MW's CGM that has been ignored in previous studies.

In conducting this study, we perform continuum normalization for a total of 401 QSO spectra (§ 2.1) observed with HST/COS, which is based on a subset of HSLA (Peeples et al. 2017). Each co-added spectrum has G130M and/or G160M gratings and has a $\text{SNR} \geq 5.0$ over the wavelength span. Our continuum normalization focuses on interstellar absorption lines, including Fe II 1142/1143/1144/1608 Å, P II 1152 Å, S II 1250/1253/1259 Å, Si II 1190/1193/1206/1526 Å, Si III 1260 Å, Si IV 1393/1402 Å, C II 1334 Å, and C IV 1548/1550 Å. For each QSO we also retrieve H I 21cm emission lines from three H I surveys: GALFA-H I (Peek et al. 2018), LAB (Kalberla et al. 2005), and HI4PI (HI4PI Collaboration et al. 2016). The QSO continua, individual line spectra, and the corresponding H I 21cm lines together form our COS-GAL dataset, which we release to the public at [10.17909/T9N677] (§ 2.2).

Critical information is missing when relying on QSO sightlines to probe the MW halo – the distance. For future studies, we will add in new halo star samples to constraint the distance to the Si IV content associated with the MW's disk-halo interface, thus shed light on the location of the low-intermediate velocity gas hidden in

the MW's CGM. In future applications of the COS-GAL dataset, we will use other ions present in the COS spectra to study the MW's disk-halo and halo. Our COS-GAL dataset has broad potential usage, such as studying the global phenomena of ionized HVCs, gas flows in different directions, the ionized gas properties in specific regions of the MW, or the surroundings of galaxies in the Local Group.

Acknowledgement. We are very grateful to B. Wakker and B. Savage for pointing out a critical systemic error in calculating the Si IV apparent column density in the previous version of this manuscript. We thank K. Tchernyshyov for useful discussions on COS ion absorption lines and apparent column density profile derivations. We thank M. Peebles for answering many of our questions about HSLA. We thank S. Flemming for assisting us in turning the COS-GAL dataset into a high-level science product hosted at the Mikulski Archive for Space Telescopes (MAST). We acknowledge support from HST-GO-13706, HST-GO-13383, and HST-GO-13382 which were provided by NASA through grants from the Space Telescope Science Institute (STScI). STScI is operated by the Association of Universities for Research in Astronomy, Inc., under NASA contract NAS5-26555. Most of the data presented in this paper were obtained from the MAST. We also acknowledge support from the National Science Foundation under Grant No. AST-1410800 and AST-1312888.

Software: Astropy (Astropy Collaboration et al. 2013), Linetools (Prochaska et al. 2016), IPython package (Pérez & Granger 2007), matplotlib (Hunter 2007).

REFERENCES

- Ackermann, M., Albert, A., Atwood, W. B., et al. 2014, ApJ, 793, 64
- Albert, C. E., & Danly, L. 2004, in Astrophysics and Space Science Library, Vol. 312, High Velocity Clouds, ed. H. van Woerden, B. P. Wakker, U. J. Schwarz, & K. S. de Boer, 73
- Allen, J. T., Schaefer, A. L., Scott, N., et al. 2015, MNRAS, 451, 2780
- Anderson, M. E., & Bregman, J. N. 2010, ApJ, 714, 320
- Asplund, M., Grevesse, N., Sauval, A. J., & Scott, P. 2009, ARA&A, 47, 481
- Astropy Collaboration, Robitaille, T. P., Tollerud, E. J., et al. 2013, A&A, 558, A33
- Bizyaev, D., Waltherbos, R. A. M., Yoachim, P., et al. 2017, ApJ, 839, 87
- Boettcher, E., Zweibel, E. G., Gallagher, III, J. S., & Benjamin, R. A. 2016, ApJ, 832, 118
- Bordoloi, R., Tumlinson, J., Werk, J. K., et al. 2014, ApJ, 796, 136
- Bordoloi, R., Fox, A. J., Lockman, F. J., et al. 2017, ApJ, 834, 191
- Bowen, D. V., Jenkins, E. B., Tripp, T. M., et al. 2008, ApJS, 176, 59
- Bundy, K., Bershady, M. A., Law, D. R., et al. 2015, ApJ, 798, 7
- Burchett, J. N., Tripp, T. M., Bordoloi, R., et al. 2016, ApJ, 832, 124

- Chen, H.-W., Helsby, J. E., Gauthier, J.-R., et al. 2010, *ApJ*, 714, 1521
- Collins, J. A., Shull, J. M., & Giroux, M. L. 2009, *ApJ*, 705, 962
- Dickey, J. M., & Lockman, F. J. 1990, *ARA&A*, 28, 215
- Ferland, G. J., Korista, K. T., Verner, D. A., et al. 1998, *PASP*, 110, 761
- Ferland, G. J., Porter, R. L., van Hoof, P. A. M., et al. 2013, *Rev. Mexicana Astron. Astrofis.*, 49, 137
- Fox, A. J., Savage, B. D., & Wakker, B. P. 2006, *ApJS*, 165, 229
- Fox, A. J., Wakker, B. P., Savage, B. D., et al. 2005, *ApJ*, 630, 332
- Fox, A. J., Bordoloi, R., Savage, B. D., et al. 2015, *ApJL*, 799, L7
- Fraternali, F., Oosterloo, T. A., Sancisi, R., & Swaters, R. 2005, in *Astronomical Society of the Pacific Conference Series*, Vol. 331, *Extra-Planar Gas*, ed. R. Braun, 239
- Gnat, O., & Sternberg, A. 2007, *ApJS*, 168, 213
- Gupta, A., Mathur, S., Krongold, Y., Nicastro, F., & Galeazzi, M. 2012, *ApJL*, 756, L8
- Haardt, F., & Madau, P. 2001, in *Clusters of Galaxies and the High Redshift Universe Observed in X-rays*, ed. D. M. Neumann & J. T. V. Tran, 64
- HI4PI Collaboration, Ben Bekhti, N., Flöer, L., et al. 2016, *A&A*, 594, A116
- Ho, I.-T., Medling, A. M., Bland-Hawthorn, J., et al. 2016, *MNRAS*, 457, 1257
- Howk, J. C., Sembach, K. R., & Savage, B. D. 2006, *ApJ*, 637, 333
- Hunter, J. D. 2007, *Computing In Science & Engineering*, 9, 90
- Jenkins, E. B. 1978, *ApJ*, 219, 845
- Joung, M. R., Putman, M. E., Bryan, G. L., Fernández, X., & Peek, J. E. G. 2012, *ApJ*, 759, 137
- Kalberla, P. M. W., Burton, W. B., Hartmann, D., et al. 2005, *A&A*, 440, 775
- Keeney, B. A., Stocke, J. T., Danforth, C. W., et al. 2017, *ApJS*, 230, 6
- Lehner, N., & Howk, J. C. 2007, *MNRAS*, 377, 687
- Lehner, N., Howk, J. C., Thom, C., et al. 2012, *MNRAS*, 424, 2896
- Lehner, N., Howk, J. C., & Wakker, B. P. 2015, *ApJ*, 804, 79
- Levine, E. S., Blitz, L., & Heiles, C. 2006, *ApJ*, 643, 881
- Levine, E. S., Heiles, C., & Blitz, L. 2008, *ApJ*, 679, 1288
- Liang, C. J., & Chen, H.-W. 2014, *MNRAS*, 445, 2061
- Marasco, A., & Fraternali, F. 2011, *A&A*, 525, A134
- Marasco, A., Fraternali, F., & Binney, J. J. 2012, *MNRAS*, 419, 1107
- Morton, D. C. 2003, *ApJS*, 149, 205
- Nicastro, F., Zezas, A., Elvis, M., et al. 2003, *Nature*, 421, 719
- Peek, J. E. G., Heiles, C., Putman, M. E., & Douglas, K. 2009, *ApJ*, 692, 827
- Peek, J. E. G., Babler, B. L., Zheng, Y., et al. 2018, *ApJS*, 234, 2
- Peeples, M., Tumlinson, J., Fox, A., et al. 2017, *The Hubble Spectroscopic Legacy Archive*, Tech. rep.
- Pérez, F., & Granger, B. E. 2007, *Computing in Science and Engineering*, 9, 21
- Prochaska, J. X., Tejos, N., Crighton, N., Burchett, J., & Tuo-Ji. 2016, *linetools/linetools: Second major release, v.v0.2*, Zenodo, doi:10.5281/zenodo.168270
- Prochaska, J. X., Weiner, B., Chen, H.-W., Mulchaey, J., & Cooksey, K. 2011, *ApJ*, 740, 91
- Prochaska, J. X., Werk, J. K., Worseck, G., et al. 2017, *ApJ*, 837, 169
- Putman, M. E., Peek, J. E. G., & Joung, M. R. 2012, *ARA&A*, 50, 491
- Rand, R. J. 1997, *ApJ*, 474, 129
- . 2000, *ApJL*, 537, L13
- Richter, P., Nuza, S. E., Fox, A. J., et al. 2017, *A&A*, 607, A48
- Saul, D. R., Peek, J. E. G., & Putman, M. E. 2014, *MNRAS*, 441, 2266
- Savage, B. D., Edgar, R. J., & Diplas, A. 1990, *ApJ*, 361, 107
- Savage, B. D., & Lehner, N. 2006, *ApJS*, 162, 134
- Savage, B. D., & Sembach, K. R. 1991, *ApJ*, 379, 245
- . 1996, *ARA&A*, 34, 279
- Savage, B. D., Sembach, K. R., & Lu, L. 1997, *AJ*, 113, 2158
- Savage, B. D., & Wakker, B. P. 2009, *ApJ*, 702, 1472
- Savage, B. D., Sembach, K. R., Wakker, B. P., et al. 2003, *ApJS*, 146, 125
- Shapiro, P. R., & Field, G. B. 1976, *ApJ*, 205, 762
- Shull, J. M., Jones, J. R., Danforth, C. W., & Collins, J. A. 2009, *ApJ*, 699, 754
- Stocke, J. T., Keeney, B. A., Danforth, C. W., et al. 2013, *ApJ*, 763, 148
- Tumlinson, J., Peeples, M. S., & Werk, J. K. 2017, *ARA&A*, 55, 389
- Tumlinson, J., Thom, C., Werk, J. K., et al. 2011, *Science*, 334, 948
- van Woerden, H., Wakker, B. P., Schwarz, U. J., & de Boer, K. S., eds. 2004, *Astrophysics and Space Science Library*, Vol. 312, *High Velocity Clouds*
- Wakker, B. P. 1991, in *IAU Symposium*, Vol. 144, *The Interstellar Disk-Halo Connection in Galaxies*, ed. H. Bloemen, 27–40
- Wakker, B. P. 2004, in *Astrophysics and Space Science Library*, Vol. 312, *High Velocity Clouds*, ed. H. van Woerden, B. P. Wakker, U. J. Schwarz, & K. S. de Boer, 25
- Wakker, B. P., Kalberla, P. M. W., van Woerden, H., de Boer, K. S., & Putman, M. E. 2001, *ApJS*, 136, 537
- Wakker, B. P., Savage, B. D., Fox, A. J., Benjamin, R. A., & Shapiro, P. R. 2012, *ApJ*, 749, 157
- Werk, J. K., Prochaska, J. X., Tumlinson, J., et al. 2014, *ApJ*, 792, 8
- Werk, J. K., Prochaska, J. X., Cantalupo, S., et al. 2016, *ApJ*, 833, 54
- Zheng, Y., Putman, M. E., Peek, J. E. G., & Joung, M. R. 2015, *ApJ*, 807, 103

Table 1: Si IV Data Sample

No.	HSLA-ID	l ($^{\circ}$)	b ($^{\circ}$)	RA ($^{\circ}$)	DEC ($^{\circ}$)	z	SNR (per pix)	Q	$\log N_{1393}$	$v_{c,1393}$ km s $^{-1}$	$\log N_{1402}$	$v_{c,1402}$ km s $^{-1}$
(0)	(1)	(2)	(3)	(4)	(5)	(6)	(7)	(8)	(9)	(10)	(11)	(12)
1 †	NGC-5548	31.96	70.50	214.50	25.14	0.017	62.7	0	13.75 \pm 0.00	-42.7 \pm 0.3	13.75 \pm 0.00	-44.7 \pm 0.5
2 †	MARK509	35.97	-29.86	311.04	-10.72	0.034	37.8	0	13.82 \pm 0.00	24.2 \pm 0.3	13.82 \pm 0.00	27.6 \pm 0.6
3 *	MRK876	98.27	40.38	243.49	65.72	0.129	34.6	0	13.64 \pm 0.00	-24.5 \pm 0.5	13.64 \pm 0.01	-19.9 \pm 1.0
4 *	RXJ1230.8+0115	291.26	63.66	187.71	1.26	0.117	25.1	0	13.51 \pm 0.01	-4.6 \pm 0.8	13.51 \pm 0.01	-4.3 \pm 1.7
5	PG0804+761	138.28	31.03	122.74	76.04	0.100	24.2	0	13.55 \pm 0.01	-39.7 \pm 1.0	13.56 \pm 0.01	-39.8 \pm 2.0
6 *	NGC-7469	83.10	-45.47	345.82	8.87	0.016	23.6	0	13.48 \pm 0.01	3.3 \pm 1.0	13.49 \pm 0.01	-1.0 \pm 1.8
7	IRAS-F22456-5125	338.51	-56.63	342.17	-51.16	0.100	19.1	0	13.32 \pm 0.01	9.1 \pm 1.6	13.33 \pm 0.03	10.9 \pm 3.4
8	PG1116+215	223.36	68.21	169.79	21.32	0.176	19.1	0	13.66 \pm 0.01	-12.8 \pm 0.9	13.66 \pm 0.01	-12.1 \pm 1.5
9 *	PKS2155-304	17.73	-52.25	329.72	-30.23	0.116	18.6	0	13.35 \pm 0.01	2.6 \pm 1.7	13.36 \pm 0.02	-1.0 \pm 3.1
10 †	PG1352+183	4.37	72.87	208.65	18.09	0.152	18.1	0	13.61 \pm 0.01	-33.6 \pm 1.4	13.60 \pm 0.02	-36.0 \pm 2.5
11	IO-AND	122.28	-23.18	12.08	39.69	0.134	17.5	0	13.16 \pm 0.02	-25.5 \pm 2.8	13.20 \pm 0.04	-15.1 \pm 4.8
12	IRAS-L06229-6434	274.31	-27.32	95.78	-64.61	0.128	17.3	0	13.31 \pm 0.02	15.9 \pm 2.2	13.31 \pm 0.03	24.5 \pm 4.3
13	MRK817	100.30	53.48	219.09	58.79	0.031	17.2	0	13.44 \pm 0.01	-34.2 \pm 1.7	13.42 \pm 0.02	-34.1 \pm 3.5
14 *	TONS210	224.97	-83.16	20.46	-28.35	0.116	16.8	0	13.54 \pm 0.01	-14.4 \pm 1.2	13.53 \pm 0.02	-10.4 \pm 2.5
15	NGC-985	180.84	-59.49	38.66	-8.79	0.042	16.5	0	13.35 \pm 0.01	-38.3 \pm 2.2	13.36 \pm 0.03	-30.7 \pm 4.0
16	PG0052+251	123.91	-37.44	132.72	25.43	0.154	16.3	0	13.27 \pm 0.02	-10.7 \pm 2.5	13.29 \pm 0.03	-15.4 \pm 3.4
17 *	PHL1811	47.47	-44.82	328.76	-9.37	0.190	16.1	0	13.59 \pm 0.01	3.2 \pm 1.1	13.59 \pm 0.02	3.5 \pm 2.1
18 *	HE0226-4110	253.94	-65.77	37.06	-40.95	0.493	14.8	0	13.36 \pm 0.02	0.1 \pm 2.0	13.38 \pm 0.03	4.9 \pm 3.9
19	PG-1407+265	34.67	72.59	212.35	26.31	0.940	14.7	0	13.75 \pm 0.01	-43.7 \pm 1.3	13.75 \pm 0.01	-41.8 \pm 2.2
20	FAIRALL9	295.07	-57.83	20.94	-58.81	0.047	14.5	0	13.47 \pm 0.01	12.2 \pm 1.7	13.47 \pm 0.03	18.6 \pm 3.5
21	3C263	134.16	49.74	174.99	65.80	0.646	14.5	0	13.65 \pm 0.01	-47.7 \pm 1.7	13.66 \pm 0.02	-41.3 \pm 2.7
22 *	PG0953+414	179.79	51.71	149.22	41.26	0.234	14.4	0	13.39 \pm 0.02	-21.1 \pm 2.1	13.41 \pm 0.03	-12.6 \pm 3.8
23	QSO-B1307+085	316.79	70.71	197.45	8.33	0.155	14.4	0	13.72 \pm 0.01	-21.5 \pm 1.2	13.71 \pm 0.01	-20.6 \pm 1.6
24	HE0056-3622	293.72	-80.90	14.66	-36.10	0.164	14.0	0	13.47 \pm 0.02	-10.0 \pm 1.9	13.49 \pm 0.02	-5.9 \pm 2.8
25 *	PG1259+593	120.56	58.05	195.30	59.04	0.477	13.9	0	13.33 \pm 0.02	-19.3 \pm 2.4	13.37 \pm 0.03	-10.5 \pm 4.3
26	VIIZW244	136.66	32.68	131.19	76.89	0.131	13.8	0	13.59 \pm 0.01	-43.9 \pm 1.8	13.57 \pm 0.02	-40.9 \pm 3.3
27	PG1626+554	84.51	42.19	246.98	55.38	0.133	13.8	0	13.47 \pm 0.01	-22.8 \pm 1.8	13.46 \pm 0.03	-26.9 \pm 3.8
28 †	IES1553+113	21.91	43.96	238.93	11.19	0.360	13.7	0	13.95 \pm 0.01	-2.3 \pm 0.7	13.94 \pm 0.01	-5.5 \pm 1.2
29 †	ESO-141-55	338.18	-26.71	290.31	-58.67	0.037	13.6	0	13.80 \pm 0.01	4.7 \pm 0.9	13.81 \pm 0.01	5.0 \pm 1.6
30	S50716+714	143.98	28.02	110.47	71.34	0.300	13.6	0	13.42 \pm 0.02	-39.5 \pm 2.4	13.45 \pm 0.03	-41.4 \pm 4.4

Note - Col (0): QSOs are arranged from high to low SNR per pixel. QSOs noted with * have *FUSE* spectra as used in Wakker et al. (2012) (see § 2.3), while those with † are potentially related to the Fermi Bubbles given their spatial proximity (see § 3). Col (1): QSO ID as adopted by HSLA (Peeples et al. 2017). Col (2) & (3): Galactic longitude and latitude in degree. Col (4) & (5): Right Ascension and Declination in degree. Col (6): QSO redshift as adopted by HSLA (Peeples et al. 2017). Col (7): SNR per pixel for the absorption-free region between 1394Å and 1401Å. Col (8): Quality flagging (see § 2.3): $Q = 0$ means this target has spectrally resolved doublet profiles, $Q = 1$ means its Si IV lines are likely to be saturated, and $Q = -1$ means its 1393 Å line is abnormally stronger than 1402 Å. We do not use $Q = -1$ target in our analyses. Col (9) & (10): logarithmic apparent column density and centroid velocity for Si IV 1393Å integrated from -100 to 100 km s $^{-1}$. Col (11) & (12): Same as Col (9) & (10), but for Si IV 1402 Å.

Table 2: Si IV Data Sample

No.	HSLA-ID	l (°)	b (°)	RA (°)	DEC (°)	z	SNR (per pix)	Q	$\log N_{1393}$	$v_{c,1393}$ km s ⁻¹	$\log N_{1402}$	$v_{c,1402}$ km s ⁻¹
(0)	(1)	(2)	(3)	(4)	(5)	(6)	(7)	(8)	(9)	(10)	(11)	(12)
31	SDSSJ135341.03+361948.0	71.67	73.91	208.42	36.33	0.146	13.1	0	13.35±0.02	-40.3±2.7	13.34±0.04	-48.9±7.7
32	MR2251-178	46.20	-61.33	343.52	-17.58	0.063	13.0	0	13.64±0.01	11.7±1.2	13.64±0.02	14.8±2.5
33†	LBQS-1435-0134	348.72	51.37	219.45	-1.79	1.310	12.7	0	13.69±0.01	-25.0±1.4	13.70±0.02	-22.4±2.4
34*	MRK-335	108.76	-41.42	1.58	20.20	0.025	12.5	0	13.57±0.01	-6.6±1.5	13.59±0.02	-3.7±2.7
35	IRASF00040+4325	114.42	-18.42	1.65	43.71	0.166	12.4	0	13.12±0.03	-31.0±4.9	13.13±0.05	-25.4±7.6
36	1H-2129-624	331.14	-42.52	324.10	-62.40	0.058	12.2	0	13.62±0.01	31.2±1.7	13.64±0.02	31.0±3.0
37*	NGC-3783	287.46	22.95	174.76	-37.74	0.009	12.2	0	13.75±0.01	11.8±1.1	13.73±0.02	14.8±2.0
38	MRK106	161.14	42.88	139.98	55.36	0.123	12.1	0	13.22±0.03	-20.4±3.4	13.16±0.06	-27.2±9.3
39	RXS-J23218-7026	313.29	-44.84	350.46	-70.45	0.300	11.9	0	13.62±0.01	21.2±1.5	13.63±0.02	26.4±3.0
40	RXJ2154.1-4414	355.18	-50.86	328.71	-44.23	0.344	11.7	0	13.59±0.01	22.3±1.4	13.60±0.03	29.3±3.7
41	PKS0552-640	273.47	-30.61	88.10	-64.04	0.680	11.7	0	13.38±0.02	26.5±2.8	13.35±0.04	37.0±6.1
42	HE0238-1904	200.48	-63.63	40.14	-18.86	0.631	10.8	0	13.44±0.02	-11.1±2.3	13.47±0.03	1.3±4.2
43	QSO-B0026+129	114.64	-49.25	7.31	13.27	0.142	10.8	0	13.40±0.01	-17.1±1.9	13.40±0.05	-9.9±6.1
44	MRK1513	63.67	-29.07	323.12	10.14	0.062	10.6	0	13.70±0.01	4.5±1.2	13.68±0.02	4.3±2.7
45	B0117-2837	225.73	-83.65	19.90	-28.36	0.348	10.6	0	13.55±0.02	-3.5±1.9	13.54±0.03	-3.3±4.3
46	HE0153-4520	271.80	-67.97	28.80	-45.10	0.451	10.5	0	13.38±0.02	5.5±2.7	13.41±0.04	-7.5±5.0
47	PG1126-041	267.63	52.75	172.32	-4.40	0.061	10.5	0	13.37±0.02	14.5±2.8	13.37±0.04	26.3±5.9
48	P01011-040	246.50	40.75	153.59	-4.31	0.058	10.4	0	13.37±0.02	12.1±2.9	13.36±0.04	17.6±5.9
49	2XMM-J141348.3+440014	83.83	66.35	213.45	44.00	0.089	10.2	0	13.41±0.02	-46.7±3.5	13.44±0.04	-29.3±5.7
50	RXSJ09565-0452	243.33	37.00	149.13	-4.89	0.157	10.1	0	13.65±0.01	13.3±1.9	13.65±0.02	17.5±2.8
51	RXSJ00537+2232	123.64	-40.33	13.44	22.54	0.148	10.0	0	13.38±0.02	-17.8±2.7	13.37±0.06	-26.0±8.9
52	PG0003+158	107.32	-45.33	1.50	16.16	0.450	9.9	0	13.47±0.02	11.2±2.5	13.49±0.03	0.1±4.5
53	MRK304	75.99	-34.22	334.30	14.24	0.065	9.9	0	13.78±0.01	-8.5±1.2	13.79±0.02	-6.9±2.4
54	3C-66A	140.14	-16.77	35.66	43.04	0.444	9.8	0	13.26±0.03	-23.0±4.0	13.27±0.06	-40.2±8.8
55	PG1048+342	190.60	63.44	162.93	33.99	0.167	9.8	0	13.64±0.02	-21.7±1.9	13.66±0.02	-21.1±2.9
56	3C57	173.08	-67.26	30.49	-11.54	0.670	9.8	0	13.30±0.03	-20.9±3.6	13.28±0.06	-19.3±7.7
57	RXS-J00057-5007	320.71	-65.41	1.43	-50.12	0.033	9.7	0	13.67±0.01	4.2±1.6	13.69±0.02	8.3±3.0
58	NGC-4051	148.88	70.09	180.79	44.53	0.002	9.6	0	13.50±0.02	-27.6±3.0	13.47±0.04	-29.2±5.3
59	HE2347-4342	336.03	-69.57	357.64	-43.43	2.885	9.6	0	13.24±0.03	-10.0±4.3	13.21±0.07	2.3±8.8
60	MRK1392	2.75	50.26	226.49	3.71	0.036	9.6	0	13.69±0.02	-22.5±1.7	13.71±0.02	-24.0±3.0
61	4C-0161	91.66	-60.36	357.98	-1.15	0.173	9.1	0	13.34±0.03	3.6±3.4	13.37±0.04	2.6±5.7
62	QSO-B1215+303	188.87	82.05	184.47	30.12	0.130	9.1	0	13.34±0.03	-27.3±3.7	13.38±0.05	-21.2±6.6
63*	PG1216+069	281.07	68.14	184.84	6.64	0.331	9.0	0	13.51±0.02	-5.5±2.1	13.52±0.04	-2.9±4.5
64	ESO292-G24	334.90	-68.16	356.75	-44.76	0.030	8.9	0	13.46±0.02	-13.1±2.9	13.48±0.04	-13.2±5.5
65	MRK290	91.49	47.95	233.97	57.90	0.029	8.7	0	13.48±0.02	-29.6±3.1	13.51±0.04	-17.2±5.0

Table 1 continued

Table 3: Si IV Data Sample

No.	HSLA-ID	l (°) (2)	b (°) (3)	RA (°) (4)	DEC (°) (5)	z (6)	SNR (per pix) (7)	Q (8)	$\log N_{1393}$ (9)	$v_{c,1393}$ km s ⁻¹ (10)	$\log N_{1402}$ (11)	$v_{c,1402}$ km s ⁻¹ (12)
66	RXS-J21388-3828	4.51	-48.46	324.71	-38.48	0.182	8.7	0	13.62±0.02	21.1±2.3	13.62±0.03	26.8±4.2
67	IZW1	123.75	-50.17	13.40	12.69	0.058	8.7	0	13.40±0.03	-15.5±3.3	13.39±0.05	-14.7±6.5
68	HE2258-5524	330.72	-55.67	345.47	-55.14	0.141	8.6	0	13.31±0.03	11.1±3.6	13.28±0.06	18.7±8.5
69	SDSSJ232259.98-005359.2	80.27	-56.26	350.75	-0.90	0.150	8.6	0	13.45±0.03	15.4±3.6	13.43±0.06	9.7±7.1
70	PG1222+216	255.07	81.66	186.23	21.38	0.432	8.3	0	13.45±0.03	-9.5±3.0	13.50±0.04	-7.9±5.3
71	MRK-1044	179.69	-60.48	37.52	-9.00	0.016	8.3	0	13.40±0.03	-33.5±3.9	13.45±0.04	-35.8±6.8
72	Q0439-433	247.98	-41.38	70.32	-43.23	0.593	8.0	0	13.62±0.02	1.3±2.1	13.66±0.03	-0.1±3.8
73	2MASX-J10053271-2417161	261.23	24.85	151.39	-24.29	0.153	7.8	0	13.52±0.04	30.8±5.7	13.51±0.04	35.1±5.6
74	RBS144	299.48	-65.84	15.11	-51.23	0.062	7.6	0	13.50±0.02	1.6±2.9	13.51±0.05	20.8±6.0
75	PG1001+291	200.08	53.21	151.01	28.93	0.327	7.5	0	13.62±0.02	-28.6±3.2	13.65±0.03	-25.1±4.6
76	PKS0558-504	257.96	-28.57	89.95	-50.45	0.137	7.4	0	13.69±0.02	11.1±2.2	13.72±0.03	9.5±3.6
77	RBS2055	106.67	-34.66	357.97	26.33	0.040	7.4	0	13.71±0.02	-11.8±2.0	13.72±0.03	-10.0±3.7
78	QSO-B1440+3539	59.24	65.03	220.53	35.44	0.079	7.3	0	13.49±0.03	-55.9±5.6	13.53±0.04	-46.0±6.8
79	PG1112+431	167.89	64.94	168.78	42.83	0.301	7.3	0	13.52±0.02	-38.3±3.9	13.50±0.05	-42.5±7.4
80	HS1831+5338	82.59	24.21	278.21	53.67	0.039	7.3	0	13.69±0.02	-24.8±2.6	13.68±0.03	-19.6±4.3
81	MRK1148	123.09	-45.44	12.98	17.43	0.064	7.2	0	13.35±0.03	-5.1±3.9	13.35±0.07	-20.7±9.2
82 [†]	QSO-B1617+1731	32.89	41.08	245.05	17.41	0.112	7.2	0	13.81±0.02	-23.5±2.0	13.83±0.03	-20.7±3.4
83	B0120-28	227.78	-82.93	20.65	-28.72	0.436	7.2	0	13.58±0.03	-7.7±2.8	13.61±0.04	-4.3±4.7
84	HS1102+3441	188.56	66.22	166.42	34.43	0.508	7.2	0	13.69±0.02	-24.6±2.7	13.70±0.03	-26.6±4.4
85	HB89-0232-042	174.46	-56.16	38.78	-4.03	1.437	7.1	0	13.31±0.04	-6.5±4.7	13.35±0.07	0.9±8.9
86	PG-1338+416	90.59	72.48	205.25	41.39	1.217	7.1	0	13.40±0.03	-41.0±5.3	13.33±0.07	-33.2±10.7
87*	NGC-3516	133.24	42.40	166.70	72.57	0.008	7.1	0	13.30±0.04	-51.4±7.2	13.35±0.06	-51.7±9.9
88	RBS1892	345.90	-58.37	341.33	-46.87	0.200	7.0	0	13.52±0.03	-9.7±3.2	13.55±0.04	-1.6±5.4
89 [†]	RBS1666	358.73	-31.00	301.47	-41.58	0.079	7.0	0	13.88±0.02	26.8±2.4	13.87±0.03	27.0±3.5
90	3C48	133.96	-28.72	24.42	33.16	0.367	6.9	0	13.37±0.04	-26.8±5.2	13.32±0.08	-17.5±10.2
91	PG1121+422	167.26	66.86	171.16	42.03	0.225	6.9	0	13.60±0.02	-39.2±3.9	13.64±0.04	-23.1±5.3
92	2XMM-J100420.0+051300	234.16	44.62	151.08	5.22	0.161	6.8	0	13.49±0.03	5.8±3.8	13.50±0.05	11.4±7.1
93	RXSJ00437+3725	121.23	-25.42	10.93	37.42	0.079	6.6	0	13.50±0.03	-23.9±4.1	13.49±0.06	-34.1±8.3
94 [†]	SDSSJ141542.90+163413.8	8.85	67.83	213.93	16.57	0.743	6.5	0	13.82±0.02	-37.4±3.3	13.80±0.04	-37.9±5.2
95	SDSSJ094733.21+100508.7	225.37	43.54	146.89	10.09	0.139	6.5	0	13.55±0.02	-10.5±2.9	13.58±0.05	-21.2±7.2
96	ZW535.012	120.17	-17.13	9.09	45.66	0.047	6.4	0	13.30±0.05	-15.2±5.8	13.29±0.08	-20.5±11.5
97	RBS2000	350.20	-67.58	351.19	-40.68	0.173	6.4	0	13.59±0.03	-12.5±3.1	13.63±0.05	-16.1±5.7
98	RXJ0439.6-5311	261.22	-40.93	69.91	-53.19	0.243	6.3	0	13.48±0.03	-4.7±3.6	13.52±0.06	-0.7±6.8
99	PHL2525	80.68	-71.32	0.10	-12.76	0.198	6.3	0	13.57±0.03	-20.0±3.9	13.60±0.05	-30.0±7.0
100	RXSJ00508+3536	122.80	-27.26	12.71	35.61	0.058	6.2	0	13.43±0.04	-30.1±5.2	13.42±0.07	-21.2±9.3

Table 1 continued

Table 4: Si IV Data Sample

No.	HSLA-ID	l (°) (2)	b (°) (3)	RA (°) (4)	DEC (°) (5)	z (6)	SNR (per pix) (7)	Q (8)	$\log N_{1393}$ (9)	$v_{c,1393}$ km s ⁻¹ (10)	$\log N_{1402}$ (11)	$v_{c,1402}$ km s ⁻¹ (12)
101 [†]	Q1545+210	33.90	49.46	236.93	20.87	0.264	6.0	0	13.83±0.03	-24.7±2.7	13.85±0.03	-24.2±4.2
102	TON1187	188.33	55.38	153.26	35.86	0.079	6.0	0	13.42±0.04	-27.2±5.4	13.40±0.07	-23.1±9.8
103	CAL-F-COPY	277.18	-35.42	75.77	-66.56	0.064	5.9	0	13.31±0.05	21.5±6.8	13.40±0.08	15.8±10.3
104	PMNJ1103-2329	273.19	33.08	165.91	-23.49	0.186	5.9	0	13.35±0.04	37.4±7.2	13.38±0.08	25.9±11.7
105	HB89-0107-025-NED05	134.03	-64.78	17.57	-2.31	0.956	5.9	0	13.42±0.04	-14.4±5.0	13.49±0.07	-18.9±9.2
106	SDSSJ110307.57+291230.0	201.56	66.09	165.78	29.21	0.365	5.9	0	13.44±0.04	-9.2±4.7	13.41±0.06	-16.5±8.0
107	Q0349-146	205.48	-46.32	57.87	-14.49	0.616	5.8	0	13.35±0.05	-9.5±5.4	13.38±0.08	0.1±10.1
108	QSO-B1229+204	269.44	81.74	188.01	20.16	0.063	5.8	0	13.61±0.03	-18.0±3.3	13.64±0.05	-31.1±7.2
109	FBQSJ1010+3003	198.43	54.63	152.50	30.06	0.256	5.7	0	13.51±0.04	-37.0±5.7	13.56±0.05	-36.4±8.4
110	SDSS-J141309.14+092011.2	354.10	63.76	213.29	9.34	0.460	5.6	0	13.56±0.03	-4.8±3.5	13.54±0.06	-9.3±7.2
111	HE2259-5524	330.64	-55.72	345.59	-55.14	0.854	5.6	0	13.45±0.04	11.2±4.8	13.42±0.08	12.6±9.9
112	4C25.01	114.07	-36.28	4.92	26.05	0.284	5.6	0	13.68±0.03	-15.6±3.1	13.72±0.05	-12.2±5.7
113	SDSSJ092909.79+464424.0	172.58	46.01	142.29	46.74	0.239	5.5	0	13.24±0.06	-37.2±9.8	13.28±0.10	-6.2±13.1
114	PG0923+201	210.18	42.65	141.48	19.90	0.192	5.5	0	13.17±0.07	-21.3±10.3	13.17±0.13	-31.3±18.7
115	RBS563	272.25	-39.23	69.62	-61.80	0.069	5.4	0	13.17±0.06	-0.9±7.6	13.18±0.16	6.1±21.2
116	HE0435-5304	261.02	-41.37	69.21	-52.98	1.231	5.3	0	13.32±0.05	-1.3±6.2	13.42±0.09	-14.1±12.1
117	PMNJ2345-1555	65.67	-70.99	356.30	-15.92	0.621	5.3	0	13.63±0.03	-10.4±3.5	13.66±0.05	-14.4±6.1
118	QSO-B2356-309	12.84	-78.04	359.78	-30.63	0.165	5.3	0	13.38±0.05	3.2±5.7	13.46±0.07	-5.8±9.4
119	PG0832+251	199.49	33.15	128.90	24.99	0.329	5.3	0	13.28±0.06	-15.0±7.8	13.26±0.11	0.1±14.3
120	4C-13.41	225.12	49.12	151.86	12.82	0.240	5.2	0	13.66±0.03	-0.8±3.3	13.61±0.06	12.8±7.3
121	IRAS-F04250-5718	266.99	-42.00	66.50	-57.20	0.104	30.2	1	≥13.57	-11.9±0.6	≥13.67	-10.7±1.0
122 [†]	PKS2005-489	350.37	-32.60	302.36	-48.83	0.071	8.6	1	≥14.00	41.1±2.5	≥14.06	43.4±2.5
123*	PG1211+143	267.55	74.31	183.57	14.05	0.080	7.6	1	≥13.56	-12.7±2.6	≥13.67	-3.0±3.7
124	PKS1136-13	277.53	45.43	174.79	-13.85	0.556	7.4	1	≥13.83	29.8±2.4	≥13.90	30.5±3.2
125 [†]	PG1435-067	343.98	47.21	219.57	-6.97	0.126	7.4	1	≥13.63	-35.3±3.1	≥13.69	-33.7±4.8
126	2MASS-J14312586+2442203	32.42	67.42	217.86	24.71	0.406	7.0	1	≥13.78	-39.8±3.2	≥13.87	-43.2±4.5
127	RBS2005	97.94	-36.80	351.48	21.89	0.120	6.7	1	≥13.75	2.4±1.8	≥13.90	3.1±2.8
128 [†]	MRK841	11.21	54.63	226.00	10.44	0.036	6.4	1	≥13.88	-40.0±3.5	≥14.03	-41.8±3.9
129 [†]	PDS456	10.39	11.16	262.08	-14.27	0.184	5.8	1	≥14.00	-6.4±1.9	≥14.02	1.6±2.5
130*	3C273	289.95	64.36	187.28	2.05	0.158	30.2	-1	-	-	-	0.0±0.0
131*	PKS0405-123	204.93	-41.76	61.95	-12.19	0.572	8.6	-1	-	-	-	0.0±0.0
132	TON236	44.43	55.35	232.17	28.42	0.450	7.6	-1	-	-	-	0.0±0.0

Table 1 continued